



HAL
open science

Constraining the dense matter equation of state with new NICER mass-radius measurements and new chiral effective field theory inputs

Nathan Rutherford, Melissa Mendes, Isak Svensson, Achim Schwenk, Anna L Watts, Kai Hebeler, Jonas Keller, Chanda Prescod-Weinstein, Devarshi Choudhury, Geert Raaijmakers, et al.

► To cite this version:

Nathan Rutherford, Melissa Mendes, Isak Svensson, Achim Schwenk, Anna L Watts, et al.. Constraining the dense matter equation of state with new NICER mass-radius measurements and new chiral effective field theory inputs. *Astrophys.J.Lett.*, 2024, 971 (1), pp.L19. 10.3847/2041-8213/ad5f02 . hal-04644848

HAL Id: hal-04644848

<https://hal.science/hal-04644848>

Submitted on 30 Aug 2024

HAL is a multi-disciplinary open access archive for the deposit and dissemination of scientific research documents, whether they are published or not. The documents may come from teaching and research institutions in France or abroad, or from public or private research centers.

L'archive ouverte pluridisciplinaire **HAL**, est destinée au dépôt et à la diffusion de documents scientifiques de niveau recherche, publiés ou non, émanant des établissements d'enseignement et de recherche français ou étrangers, des laboratoires publics ou privés.



Distributed under a Creative Commons Attribution 4.0 International License



Constraining the Dense Matter Equation of State with New NICER Mass–Radius Measurements and New Chiral Effective Field Theory Inputs

Nathan Rutherford¹, Melissa Mendes^{2,3,4}, Isak Svensson^{2,3,4}, Achim Schwenk^{2,3,4}, Anna L. Watts⁵, Kai Hebeler^{2,3,4}, Jonas Keller^{2,3}, Chanda Prescod-Weinstein¹, Devarshi Choudhury⁵, Geert Raaijmakers⁶, Tuomo Salmi⁵, Patrick Timmerman⁵, Serena Vinciguerra⁵, Sebastien Guillot^{7,8}, and James M. Lattimer⁹

¹ Department of Physics and Astronomy, University of New Hampshire, Durham, NH 03824, USA; nathan.rutherford@unh.edu

² Technische Universität Darmstadt, Department of Physics, 64289 Darmstadt, Germany; melissa.mendes@physik.tu-darmstadt.de, isak.svensson@physik.tu-darmstadt.de

³ ExtreMe Matter Institute EMMI, GSI Helmholtzzentrum für Schwerionenforschung GmbH, 64291 Darmstadt, Germany

⁴ Max-Planck-Institut für Kernphysik, Saupfercheckweg 1, 69117 Heidelberg, Germany

⁵ Anton Pannekoek Institute for Astronomy, University of Amsterdam, Science Park 904, 1098XH Amsterdam, The Netherlands

⁶ GRAPPA, Anton Pannekoek Institute for Astronomy and Institute of High-Energy Physics, University of Amsterdam, Science Park 904, 1098 XH Amsterdam, The Netherlands

⁷ IRAP, CNRS, 9 avenue du Colonel Roche, BP 44346, F-31028 Toulouse Cedex 4, France

⁸ Université de Toulouse, CNES, UPS-OMP, F-31028 Toulouse, France

⁹ Department of Physics and Astronomy, Stony Brook University, Stony Brook, NY 11794-3800, USA

Received 2024 April 4; revised 2024 June 28; accepted 2024 June 30; published 2024 August 8

Abstract

Pulse profile modeling of X-ray data from the Neutron Star Interior Composition Explorer is now enabling precision inference of neutron star mass and radius. Combined with nuclear physics constraints from chiral effective field theory (χ EFT), and masses and tidal deformabilities inferred from gravitational-wave detections of binary neutron star mergers, this has led to a steady improvement in our understanding of the dense matter equation of state (EOS). Here, we consider the impact of several new results: the radius measurement for the $1.42 M_{\odot}$ pulsar PSR J0437–4715 presented by Choudhury et al., updates to the masses and radii of PSR J0740+6620 and PSR J0030+0451, and new χ EFT results for neutron star matter up to 1.5 times nuclear saturation density. Using two different high-density EOS extensions—a piecewise-polytropic (PP) model and a model based on the speed of sound in a neutron star (CS)—we find the radius of a $1.4 M_{\odot}$ ($2.0 M_{\odot}$) neutron star to be constrained to the 95% credible ranges $12.28^{+0.50}_{-0.76}$ km ($12.33^{+0.70}_{-1.34}$ km) for the PP model and $12.01^{+0.56}_{-0.75}$ km ($11.55^{+0.94}_{-1.09}$ km) for the CS model. The maximum neutron star mass is predicted to be $2.15^{+0.14}_{-0.16} M_{\odot}$ and $2.08^{+0.28}_{-0.16} M_{\odot}$ for the PP and CS models, respectively. We explore the sensitivity of our results to different orders and different densities up to which χ EFT is used, and show how the astrophysical observations provide constraints for the pressure at intermediate densities. Moreover, we investigate the difference $R_{2.0} - R_{1.4}$ of the radius of $2 M_{\odot}$ and $1.4 M_{\odot}$ neutron stars within our EOS inference.

Unified Astronomy Thesaurus concepts: Gravitational wave sources (677); Neutron stars (1108); Neutron star cores (1107); X-ray sources (1822); Nuclear astrophysics (1129)

1. Introduction

The increasingly precise measurement of neutron star properties such as mass, radius, and tidal deformability, enabled by new observational facilities and techniques, informs our understanding of the equation of state (EOS) of supranuclear density matter. Radio timing measurements of high pulsar masses (Antoniadis et al. 2013; Arzoumanian et al. 2018; Cromartie et al. 2020; Fonseca et al. 2021; Shamohammadi et al. 2023) and gravitational-wave (GW) measurements of tidal deformability from neutron star binary mergers (Abbott et al. 2019, 2020) have now been supplemented by measurements of neutron star mass and radius for X-ray pulsars using data from the Neutron Star Interior Composition Explorer (NICER; Gendreau et al. 2016). These astrophysical measurements have been used in various analyses, often in combination with constraints from nuclear theory and laboratory experiments, to place limits on the properties of neutron-rich matter, possible quark or hyperon phases in neutron star cores, and the presence of dark matter in and around neutron

stars (see, e.g., Legred et al. 2021; Miller et al. 2021; Raaijmakers et al. 2021a; Biswas 2022; Huth et al. 2022; Miao et al. 2022; Annala et al. 2023; Giangrandi et al. 2023; Rutherford et al. 2023; Sun et al. 2023; Takátsy et al. 2023; Koehn et al. 2024; Kurkela et al. 2024; Pang et al. 2024; Shakeri & Karkevandi 2024).

Pulse profile modeling (PPM), the relativistic ray-tracing-based inference technique used to derive masses and radii from NICER data, is applied to X-ray-bright rotation-powered millisecond pulsars (MSPs). Full details of the PPM process can be found in Bogdanov et al. (2019, 2021). So far, mass–radius inferences have been published for the MSPs PSR J0030+0451 (hereafter, J0030; Miller et al. 2019; Riley et al. 2019) and PSR J0740+6620 (hereafter, J0740; Miller et al. 2021; Riley et al. 2021). J0030 is an isolated pulsar for which there is no independent constraint on the mass; J0740 is in a binary and the mass ($2.08 \pm 0.07 M_{\odot}$) is well constrained by radio pulsar timing (Fonseca et al. 2021). The inferred radii for these two sources have uncertainties at the $\pm 10\%$ level (68% credible interval or CI). Follow-on studies have looked more closely at specific aspects of the analysis, such as the treatment of background (Salmi et al. 2022), the atmospheric model (Salmi et al. 2023), and simulation and sampler resolution settings (Vinciguerra et al. 2023).

NICER data have now enabled inference of the mass and radius for PSR J0437–4715 (hereafter, J0437; Choudhury et al. 2024), the closest and brightest MSP. This is a challenging source to model: the presence of a bright active galactic nucleus in the field of view requires the spacecraft to observe off-axis, and despite this there is still a substantial background contribution from this source. However, J0437 is also a binary MSP with a well-constrained mass from radio pulsar timing of $M = 1.418 \pm 0.044 M_{\odot}$ (Reardon et al. 2024). The tightly constrained radio-timing-derived mass (and distance and inclination) is used as a prior for the PPM analysis, and this has enabled radius constraints at the $\pm 7\%$ level (68% CI). Precise radius information for typical $1.4 M_{\odot}$ neutron stars plays an important role for constraining the dense matter EOS, because this correlates well with the pressure of neutron-rich matter around twice saturation density (see, e.g., Lattimer & Prakash 2001; Lattimer & Lim 2013; Drischler et al. 2021a; Lim & Schwenk 2024) and thus provides key constraints at intermediate densities.

There are also new results for J0030 and J0740. Vinciguerra et al. (2024) carried out a reanalysis of the J0030 data set from Riley et al. (2019), using an upgraded PPM pipeline and instrument response model, and incorporating background constraints. This source now appears to be more complex than first thought, with different modes (corresponding to different hot spot geometries)¹⁰ that have different inferred masses and radii. Meanwhile a larger data set for J0740 has enabled more robust constraints on the mass and radius for that source (Dittmann et al. 2024; Salmi et al. 2024). This is thus an opportune moment to update our EOS analyses.

In parallel to these astrophysical advances, there have been great developments on the EOS around nuclear densities based on chiral effective field theory (χ EFT) interactions (see, e.g., Epelbaum et al. 2009; Machleidt & Entem 2011; Hammer et al. 2013; Hebeler 2021). Combined with powerful many-body methods, χ EFT interactions have enabled calculations of neutron matter up to around nuclear saturation density ($n_0 = 0.16 \text{ fm}^{-3}$) that provide important constraints for the EOS of the outer core of neutron stars (see, e.g., Hebeler et al. 2013; Lynn et al. 2019; Drischler et al. 2021b; Huth et al. 2021). In our previous multimessenger analyses (Raaijmakers et al. 2019, 2020, 2021a), we have used the χ EFT constraints from Hebeler et al. (2013), Tews et al. (2013), Lynn et al. (2016), and Drischler et al. (2019) to explore EOS inference from the NICER results derived using the X-ray Pulse Simulation and Inference (X-PSI; Riley et al. 2023) PPM pipeline (Riley et al. 2019, 2021)¹¹ in combination with GW-derived tidal deformabilities.

The EOS inference requires prior assumptions over all densities. To this end, we have used two different high-density EOS extensions—a piecewise-polytropic (PP) model (Hebeler et al. 2013) and a model based on the speed of sound in a neutron star (CS; Greif et al. 2019)—to cover the full EOS space beyond a fiducial density of $1.1n_0$, up to which the χ EFT calculations were trusted. Recently, new χ EFT calculations from Keller et al. (2023) of neutron star matter in beta

equilibrium and up to $1.5n_0$ have been presented. In this work, we explore new prior EOS ensembles based on these new χ EFT calculations at different chiral orders—next-to-next-to-leading order (N^2 LO) and next-to-next-to-next-to-leading order (N^3 LO)—as well as different transition densities ($1.1n_0$ and $1.5n_0$) to the PP and CS models.

This Letter is organized as follows. In Section 2, we introduce our Bayesian inference framework for providing constraints on the dense matter EOS and the properties of neutron stars. Sections 2.2 and 2.3 discuss the new χ EFT calculation and its implementation in our framework, as well as the new prior distributions. The astrophysical constraints are summarized in Section 2.4. In addition to a “Baseline” scenario consisting of the GW observations from GW170817 and GW190425 (Abbott et al. 2019, 2020) and the previously explored NICER sources J0740 and J0030 (Salmi et al. 2022; Vinciguerra et al. 2024), we investigate a “New” scenario with the new J0437 and J0740 NICER results (Choudhury et al. 2024; Salmi et al. 2024) and the revised analysis including background constraints for J0030 from Vinciguerra et al. (2024). Other scenarios are explored in the Appendix. In Section 3, we first study the changes due to the new priors for the “Baseline” scenario and then turn to the impact of the new observations on the dense matter EOS and the properties of neutron stars. Finally, we discuss implications and conclude in Section 4.

2. Methodology

We begin by discussing the Raaijmakers et al. (2021a) Bayesian inference framework, the new N^2 LO and N^3 LO χ EFT calculations from Keller et al. (2023) and their implementations into this framework, the resulting mass–radius and pressure–energy density prior distributions, and the usage of the available astrophysical constraints.

2.1. Bayesian Inference Framework

In this work, we follow the analysis framework used in Raaijmakers et al. (2021a), which builds on the work of Greif et al. (2019) and Raaijmakers et al. (2019, 2020). Here, we briefly summarize the method and outline any modifications. We use the open-source EOS inference code N_{Eo}ST¹² (v0.10; Raaijmakers et al. 2024), which implements this framework.¹³ A full reproduction package, including the posterior samples and scripts to generate the plots in this Letter, are available in a Zenodo repository at Rutherford et al. (2024).

For the high-density extension of the EOS, we consider two different parameterizations: (i) a PP model with three segments between varying transition densities (Hebeler et al. 2013); and (ii) a CS model first introduced in Greif et al. (2019). Below a transition density (which for our main results we take to be $1.5n_0$, but also explore the past choice of $1.1n_0$), these parameterizations are matched to a single polytropic fit to the EOS range calculated from χ EFT interactions. The latter are discussed in more detail in Section 2.2. At densities below $\approx 0.5n_0$, the χ EFT band is connected to the Baym–Pethick–Sutherland (BPS) crust EOS (Baym et al. 1971).

¹⁰ The hot spots, which give rise to the pulsation as the star rotates and the thermal emission from the magnetic poles of the star, are thought to arise due to the heat generated from magnetospheric return currents (see, e.g., Ruderman & Sutherland 1975; Harding & Muslimov 2001; Arzoumanian et al. 2018; Salmi et al. 2020).

¹¹ The results of Miller et al. (2019, 2021) are derived using an independent PPM pipeline.

¹² <https://github.com/xpsi-group/neost>

¹³ N_{Eo}ST in prerelease form was also used in Greif et al. (2019), Raaijmakers et al. (2019, 2020, 2021a), and Rutherford et al. (2023).

Using Bayes' theorem, we can write the posterior distributions of the EOS parameters θ and central energy densities ε as

$$p(\theta, \varepsilon | \mathbf{d}, \mathbb{M}) \propto p(\theta | \mathbb{M}) p(\varepsilon | \theta, \mathbb{M}) p(\mathbf{d} | \theta, \mathbb{M}), \quad (1)$$

where \mathbb{M} denotes the model including all assumed physics and \mathbf{d} the data set used to constrain the EOS, consisting of, e.g., radio, X-ray (NICER), GW, and electromagnetic counterpart (EM) data. Assuming these data sets to be independent of each other, we can separate the likelihoods and write

$$\begin{aligned} p(\theta, \varepsilon | \mathbf{d}, \mathbb{M}) &\propto p(\theta | \mathbb{M}) p(\varepsilon | \theta, \mathbb{M}) \\ &\times \prod_i p(\Lambda_{1,i}, \Lambda_{2,i}, M_{1,i}, M_{2,i} | \mathbf{d}_{\text{GW},i}, \mathbf{d}_{\text{EM},i}) \\ &\times \prod_j p(M_j, R_j | \mathbf{d}_{\text{NICER},j}) \\ &\times \prod_k p(M_k | \mathbf{d}_{\text{radio},k}). \end{aligned} \quad (2)$$

Here, $\Lambda_{1,i}$ and $\Lambda_{2,i}$ ($M_{1,i}$ and $M_{2,i}$) are the tidal deformabilities (source-frame component masses) given the GW and EM data $\mathbf{d}_{\text{GW},i}$ and $\mathbf{d}_{\text{EM},i}$. Furthermore, $\mathbf{d}_{\text{NICER},j}$ are the mass–radius (M_j – R_j) NICER data and $\mathbf{d}_{\text{radio},k}$ the mass data from radio observations. The products run over the number of different observed stars or GW mergers.

In Equation (2), we equate the nuisance-marginalized likelihoods to the nuisance-marginalized posterior distributions from the astrophysical data papers (see Raaijmakers et al. 2021a for further discussion of this issue). The posterior distributions derived from the X-PSI NICER analysis, which we use in this Letter, use a joint uniform prior in mass and radius, if not accounting for the mass prior from radio observations, where available. For a detailed discussion of how the GW parameters are handled, we refer the reader to Section 2 of Raaijmakers et al. (2021a). In order to speed up convergence, we transform the GW posterior distributions to include the two tidal deformabilities, chirp mass, and mass ratio q , fixing the chirp mass to its median value and reweighing such that the LIGO/VIRGO prior distributions on these parameters are uniform. The chirp mass is fixed to its median value because the uncertainties on this parameter are small enough to have no impact on the EOS inference (Raaijmakers et al. 2021a). By fixing the chirp mass, the central density vector ε will only have one central density per GW event considered, thus the second component's tidal deformability is now a function of the EOS parameters and the mass ratio, i.e., $\Lambda_2(\theta; q)$.

In Raaijmakers et al. (2021a), we included the constraints derived from the radio timing mass measurement of J0740, and from the EM counterpart of the event GW170817, AT2017gfo. In this work, we do not consider the radio mass measurements separately (they are instead included implicitly as priors on the mass–radius inference with NICER data). We have also chosen not to include the EM counterpart constraint, given the uncertainties in kilonova modeling (see, e.g., Raaijmakers et al. 2021b). With these changes, Equation (2) simplifies to become:

$$\begin{aligned} p(\theta, \varepsilon | \mathbf{d}, \mathbb{M}) &\propto p(\theta | \mathbb{M}) p(\varepsilon | \theta, \mathbb{M}) \\ &\times \prod_i p(\Lambda_{1,i}, \Lambda_{2,i}, q_i | \mathcal{M}_c, \mathbf{d}_{\text{GW},i}) \\ &\times \prod_l p_{\text{new}}(M_l, R_l | \mathbf{d}_{\text{NICER}+\text{radio},l}), \end{aligned} \quad (3)$$

where $p_{\text{new}}(M_l, R_l | \mathbf{d}_{\text{NICER}+\text{radio},l})$ is the redefined NICER likelihood function, with the radio observations included in the

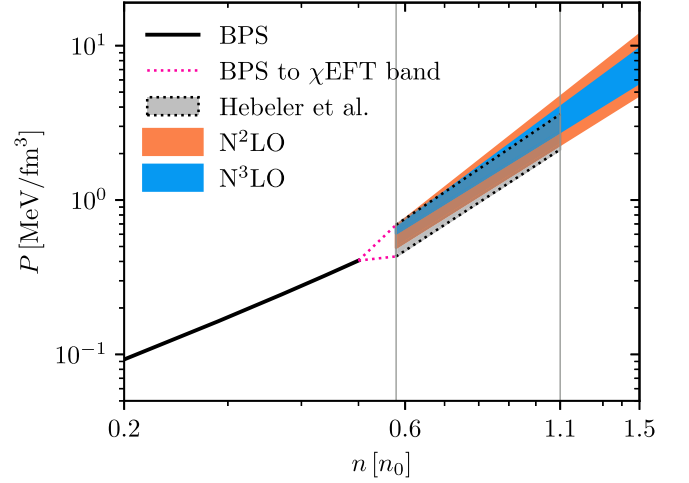


Figure 1. Pressure P as a function of density n for matter in beta equilibrium based on the new χ EFT calculations at N^2 LO (orange) and N^3 LO (blue) from Keller et al. (2023; including contributions from electrons and muons) compared to those from Hebeler et al. (2013; dotted gray). We also show the BPS crust EOS (solid black) and the polytropic interpolation of the BPS EOS to the χ EFT band (dotted pink). The beginning of the χ EFT bands is shown as a gray vertical line at $n = 0.5792n_0$, and a second vertical line indicates $n = 1.1n_0$. For simplicity, we only show the BPS EOS to the Hebeler et al. (2013) χ EFT matching, but the transitions to the Keller et al. (2023) N^2 LO and N^3 LO bands are performed using an identical procedure.

prior of $\mathbf{d}_{\text{NICER}+\text{radio},l}$ in the cases of J0740 and J0437. With Equation (3) in hand, we sample from the prior distribution $p(\theta | \mathbb{M})p(\varepsilon | \theta, \mathbb{M})$, compute the corresponding M , R , and Λ , and then evaluate the likelihood by applying a kernel density estimation to the posterior distributions from the astrophysical analyses using the nested sampling software MULTINEST (Feroz et al. 2009; Buchner et al. 2014). Some modifications are made to the prior distributions of $p(\theta | \mathbb{M})$ to accommodate the new χ EFT calculations; these are described in more detail in the following section.

2.2. New χ EFT Constraints and Implementation

In previous works, the χ EFT calculations needed to be combined with an empirical parameterization (Hebeler et al. 2013) to go from pure neutron matter to matter in beta equilibrium with a small proton fraction of $\sim 5\%$. The resulting pressure P as a function of density n is shown for the Hebeler et al. (2013) χ EFT band in Figure 1. As can be seen, the pressure increases to a very good approximation linearly on this log-plot, so that within the χ EFT band it can be described by a single polytrope varying between the minimum and maximum extent of the pressure band.

Figure 1 also shows the new χ EFT calculations at N^2 LO and N^3 LO from Keller et al. (2023), which are determined directly in beta equilibrium without the need for an empirical parameterization. Since the bands extend to higher densities $n \leq 1.5n_0$, these results also include the small contribution of muons (in addition to electrons) for the pressure of the neutron star matter in Figure 1 (Keller 2023; see, e.g., Essick et al. 2021 for the inclusion of muons). As is evident from Figure 1, the new N^2 LO and N^3 LO χ EFT bands can also be effectively parameterized with a single polytrope. This is not surprising, because the density range over which we use χ EFT is small (from $0.5 - 1.5n_0$). Moreover, around n_0 , the density dependence of the pressure is dominated by three-nucleon interactions

and in particular the large c_3 coupling contribution (see, e.g., Hebeler & Schwenk 2010; Tews et al. 2013). Thus, variations of the χ EFT interactions will give similar density dependencies within the minimum and maximum of the χ EFT band, and because of the limited density range they can again be represented by a single polytrope.

In order to implement the new χ EFT results into the NEoST framework, we therefore fit a single polytrope $P(n) = K(n/n_0)^\Gamma$ to the lower and upper pressure limits over the entire density range $0.5 \leq n/n_0 \leq 1.5$. Here, K is a constant and Γ is the polytropic index. We find that the N²LO χ EFT band is well reproduced by $K \in [1.814, 3.498] \text{ MeV fm}^{-3}$ and $\Gamma \in [2.391, 3.002]$ and the N³LO χ EFT band by $K \in [2.207, 3.056] \text{ MeV fm}^{-3}$ and $\Gamma \in [2.361, 2.814]$. As discussed above, for densities below $n \leq 0.5n_0$, the BPS crust is used, with a log-linear interpolation to the first χ EFT data points at $0.5792n_0$ for the Hebeler et al. (2013) band. We have checked that this procedure also works for the new χ EFT results, which are also log-linearly interpolated to the BPS crust at $0.5792n_0$, ensuring that the pressure is never decreasing between the BPS crust and the χ EFT band. This matching between the BPS crust and the χ EFT bands is illustrated in Figure 1.

2.3. New Prior Distributions

To generate the PP model, the three polytropic indices are varied within the ranges $\Gamma_1 \in [1, 4.5]$, $\Gamma_2 \in [0, 8]$, and $\Gamma_3 \in [0.5, 8]$, where the first polytrope goes from $1.1n_0$ to $n_1 \in [1.5, 8.3]n_0$, the second segment from n_1 to $n_2 \in [1.5, 8.3]n_0$, and the third from n_2 to the maximal central density, when the χ EFT band is used up to $1.1n_0$ (for details, see Hebeler et al. 2013). When the χ EFT band is extended to $1.5n_0$, the parameter ranges are accordingly increased, such that $\Gamma_1 \in [0, 8]$, $n_1 \in [2, 8.3]n_0$, and $n_2 \in [2, 8.3]n_0$. Note that the first polytropic index was restricted in Hebeler et al. (2013) to limit the EOS variation in the first segment just above the saturation density to reasonable density dependencies. When using χ EFT up to $1.5n_0$, we remove this limitation. For the EOS and neutron star inference, the pressure as a function of energy density is calculated from the polytropes in number density or mass density using thermodynamic relations (for details, see Read et al. 2009).¹⁴

The speed of sound parameterization (CS) follows the model detailed in Greif et al. (2019), where $c_s^2 = dP/d\varepsilon$ and

$$c_s^2(x)/c^2 = a_1 e^{-\frac{1}{2}(x-a_2)^2/a_3^2} + a_6 + \frac{\frac{1}{3} - a_6}{1 + e^{-a_5(x-a_4)}}, \quad (4)$$

with $x = \varepsilon/(m_N n_0)$ and the nucleon mass $m_N = 939.565 \text{ MeV}$. The parameters a_1 to a_5 vary within the ranges of $a_1 \in [0.1, 1.5]$, $a_2 \in [1.5, 12]$, $a_3 \in [0.075, 24]$, $a_4 \in [1.5, 37]$, and $a_5 \in [0.1, 1]$, and a_6 is fixed to continuously match to the χ EFT-band polytrope. Further constraints are implemented to guarantee that only EOSs that are causal, $0 \leq c_s^2 \leq c^2$, are included and that the speed of sound approaches the asymptotic

value of $c_s^2 = c^2/3$ from below. Moreover, we require the speed of sound up to $1.5n_0$ to not exceed a limit motivated by Fermi liquid theory (for details, see Greif et al. 2019):

$$c_s^2(1.5n_0)/c^2 \leq \frac{1}{m_N^2} (3\pi^2 n)^{2/3}. \quad (5)$$

This is automatically fulfilled for the new χ EFT calculations up to $1.5n_0$. For the pressure as a function of the energy density needed to solve the Tolman–Oppenheimer–Volkov (TOV) equations (to obtain mass and radius), we use the same prescription for the polytropes up to the end of the χ EFT band as for the PP model, and then integrate the speed of sound squared $dP/d\varepsilon = c_s^2$, matching to the energy density and with ε as a continuous variable for higher densities. Note that for both the PP and CS models, we have made the choice to sample uniformly in the space of the EOS parameters. Finally, as previously described in Hebeler et al. (2013), Greif et al. (2019), and Raaijmakers et al. (2020), the PP and CS models explicitly allow for first-order phase transitions (with $\Gamma = 0$ in PP and a region of $c_s^2 = 0$ in CS).

Implementing the N²LO and N³LO χ EFT bands generates the 68% and 95% credible region contours of the prior distributions displayed in Figure 2 for mass and radius and Figure 3 for pressure and energy density. The upper panels in both figures show the case when the new χ EFT bands are used up to $1.1n_0$, as well as a comparison based on the Hebeler et al. (2013) band (also up to $1.1n_0$), which was used in our previous EOS inference work (Raaijmakers et al. 2019, 2020, 2021a). The lower panels display the prior distributions obtained when using the new χ EFT bands up to $1.5n_0$. All the priors and the resulting posteriors were calculated for neutron stars with masses $M \geq 1.0 M_\odot$; this is theoretically motivated by the description of the early evolution of a neutron star (Strobel et al. 1999) and in agreement with neutron star minimum remnant masses from core-collapse supernova simulations (Janka et al. 2008; Fischer et al. 2010; Radice et al. 2017; Suwa et al. 2018).¹⁵

Overall, the prior distributions are similar, considering the large range in mass–radius and pressure–energy density. Compared to our previous work using the Hebeler et al. (2013) band, the new N²LO and N³LO χ EFT bands shift the mass–radius priors to slightly larger radii. This is consistent with the larger pressures for the new χ EFT bands in Figure 1. As we increase the transition density to $1.5n_0$, the prior ranges are narrowed, while keeping similar distributions and mean values for radii. Finally, the prior distributions for the pressure and energy density in Figure 3 naturally show similar results as for the mass–radius priors, with the tightest credible regions coming from the new χ EFT bands trusted up to $1.5n_0$ for both the PP and CS parameterizations.

Since the Keller et al. (2023) N³LO χ EFT band gives the tightest constraints, with consistent and similar results for the Hebeler et al. (2013) and Keller et al. (2023) N²LO bands, our analysis from here on will focus on the N³LO χ EFT band up to the transition densities $1.1n_0$ and $1.5n_0$. Results for the Hebeler

¹⁴ We note that as a result of the pressure and number density (or mass density) being the continuous variable in the PP model, the energy density and the chemical potentials are not continuous at the transition between polytropes. However, this has a small effect on bulk properties, such as mass and radius. In Hebeler et al. (2013), we explored this explicitly for the crust-to- χ EFT matching. Note that the current choice also makes it possible to compare with our previous results. However, this can be improved in the future, e.g., using a generalized PP parameterization (O’Boyle et al. 2020).

¹⁵ While recent spectral modeling of G353.6–0.7 has hinted at the possibility of lower-mass neutron stars (Doroshenko et al. 2022), this interpretation relies on several critical assumptions (on the distance to the star, which assumes some association with a candidate binary companion, as well as on the spectral modeling of the object and the data sets chosen for the analysis) and is disputed by Alford & Halpern (2023).

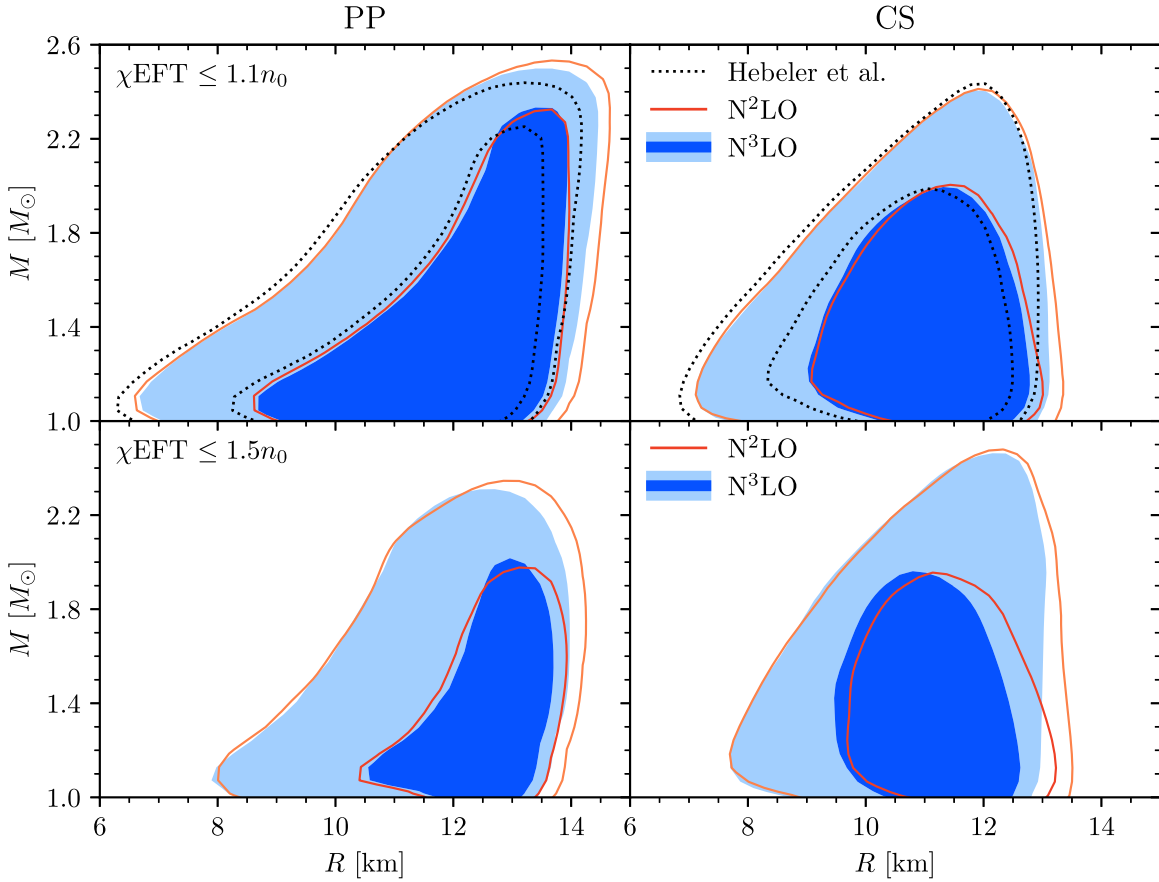


Figure 2. Mass–radius prior distributions for the PP model (left panels) and CS model (right panels). The dark (light) blue region and the inner (outer) curves encompass the 68% (95%) credible regions. The top panels compare the priors based on the new χ EFT calculations at N²LO (red) and N³LO (blue) from Keller et al. (2023) to those based on the χ EFT calculations from Hebeler et al. (2013; dotted black). For the top panels, the χ EFT bands are used up to $1.1n_0$. In the bottom panels, the prior distributions are shown when using the new χ EFT calculations up to $1.5n_0$.

et al. (2013) and Keller et al. (2023) N²LO χ EFT bands are provided in the Appendix.

2.4. Constraints from Astrophysical Data Sets

In Raaijmakers et al. (2021a), we used the following NICER mass–radius and GW mass–tidal deformability posteriors as inputs for our analysis:

1. The mass and radius for J0030 reported by Riley et al. (2019), using the 2017–2018 NICER data set and the preferred ST+PST¹⁶ model (68% CIs $M = 1.34_{-0.16}^{+0.15} M_\odot$ and $R = 12.71_{-1.19}^{+1.14}$ km).
2. The mass and radius for J0740 reported by Riley et al. (2021) from joint modeling of NICER and XMM data, using NICER data from 2018 to 2020 and the radio-derived mass as a prior, for the preferred ST-U model (68% CIs $M = 2.08 \pm 0.07 M_\odot$ and $R = 12.39_{-0.98}^{+1.30}$ km).
3. The masses and tidal deformabilities for GW170817 (Abbott et al. 2019) and GW190425 (Abbott et al. 2020).

To assess the effect of updating our EOS priors and to provide a good baseline for assessing the impact of the new data sets and analyses, we first carry out runs with the older

astrophysical inputs, with some small changes. For J0030, we replace the mass and radius posteriors from Riley et al. (2019) with the posteriors from the ST+PST NICER-only analysis of the same data set from Vinciguerra et al. (2024; 68% CIs $M = 1.37 \pm 0.17 M_\odot$ and $R = 13.11 \pm 1.30$ km), since these were obtained with an improved analysis pipeline and settings. For J0740, we replace the mass and radius posteriors from Riley et al. (2021) with those from Salmi et al. (2022), which treat the background more thoroughly (68% CIs $M = 2.07 \pm 0.07 M_\odot$ and $R = 12.97_{-1.39}^{+1.56}$ km). We select the “3C50-3X” case using only NICER data with the 3C50 model (Remillard et al. 2022), setting a lower limit to the background. Together with the GW mass–tidal deformability posteriors, these form the “Baseline” astrophysical scenario in Table 2.

We then have several new NICER mass–radius posteriors whose impact we can assess. As in our previous papers, we use results from the X-PSI PPM analysis.¹⁷ For the high-mass pulsar J0740, we use the inferred mass and radius resulting from joint NICER and XMM analysis, using the 2018–2022 NICER set reported by Salmi et al. (2024; 68% CIs $M = 2.07 \pm 0.07 M_\odot$ and $R = 12.49_{-0.88}^{+1.28}$ km). For the $1.4 M_\odot$ pulsar J0437, we use the mass–radius posterior obtained by Choudhury et al. (2024), using the 2017–2021 NICER data set, for the preferred CST+PDT model and taking into account

¹⁶ ST-U, ST+PST, ST+PDT, and PDT-U are different models used in X-PSI that describe the shape and temperature distribution assumed for the hot X-ray-emitting spots. For a schematic that illustrates the different models, see Figure 1 of Vinciguerra et al. (2023).

¹⁷ These are derived using a jointly uniform prior distribution on mass and radius (when neglecting the mass prior from radio observations), as discussed in Raaijmakers et al. (2018) and Riley et al. (2018).

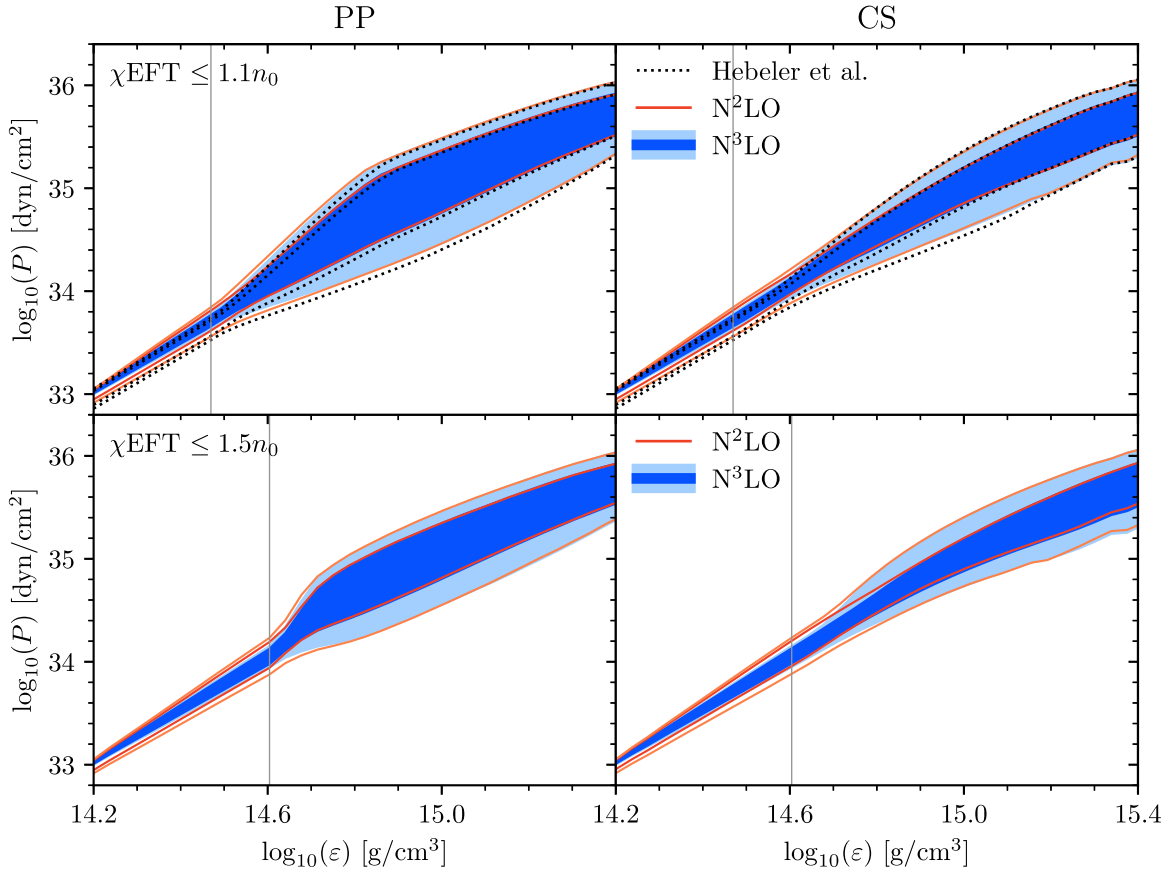


Figure 3. The same as Figure 2, but for the pressure–energy density prior distributions. The vertical thin lines mark the transition density to the high-density PP and CS extensions.

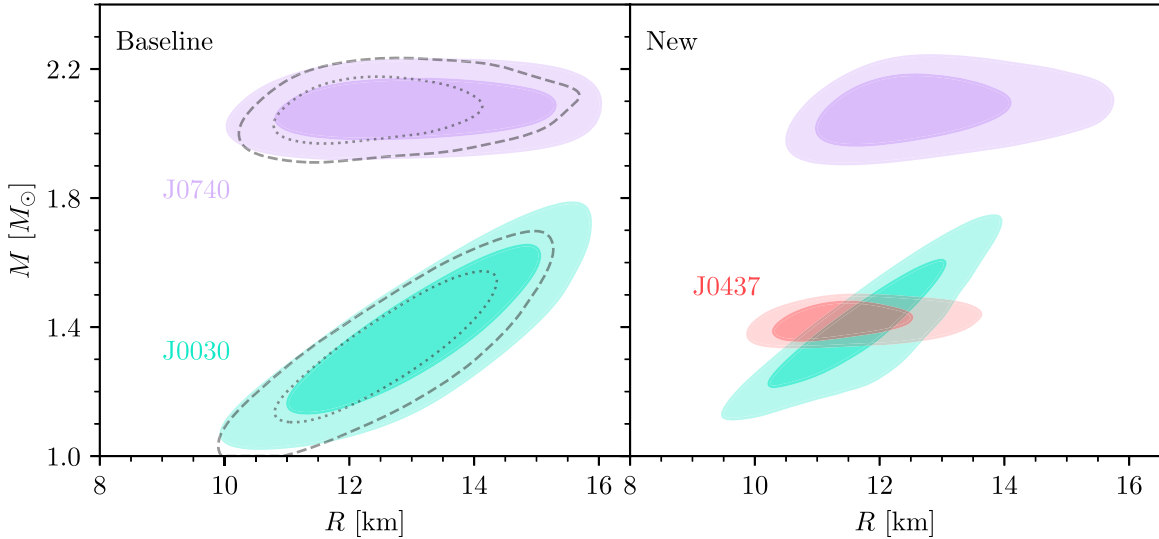


Figure 4. Overview of NICER sources (68% and 95% credible regions for mass–radius) for the “Baseline” scenario (J0740 results from Salmi et al. 2022 and J0030 NICER-only results from Vinciguerra et al. 2024) and the “New” scenario (J0437 results from Choudhury et al. 2024, J0740 results from Salmi et al. 2024, and the ST+PDT solution for J0030, including background constraints, from Vinciguerra et al. 2024). For the “Baseline” scenario, we show for comparison the 68% (95%) credible regions from Riley et al. (2021) and Riley et al. (2019) as dotted (dashed) lines, which were used in Raaijmakers et al. (2021a).

limits on the nonsource background (68% CIs $M = 1.42 \pm 0.04 M_{\odot}$ and $R = 11.36^{+0.95}_{-0.63}$ km).

For J0030, we consider three alternative sets of mass–radius posteriors from the reanalysis of the 2017–2018 data set reported by Vinciguerra et al. (2024), which supersedes the results of Riley et al. (2019). In addition to the ST+PST

NICER-only result used in the “Baseline” case, we also consider the two modes preferred in the joint analysis of NICER and XMM data (with XMM being used to place constraints on the nonsource background): ST+PDT (68% CIs $M = 1.40^{+0.13}_{-0.12} M_{\odot}$ and $R = 11.71^{+0.88}_{-0.83}$ km) and PDT-U (68% CIs $M = 1.70^{+0.18}_{-0.19} M_{\odot}$ and $R = 14.44^{+0.88}_{-1.05}$ km). PDT-U is

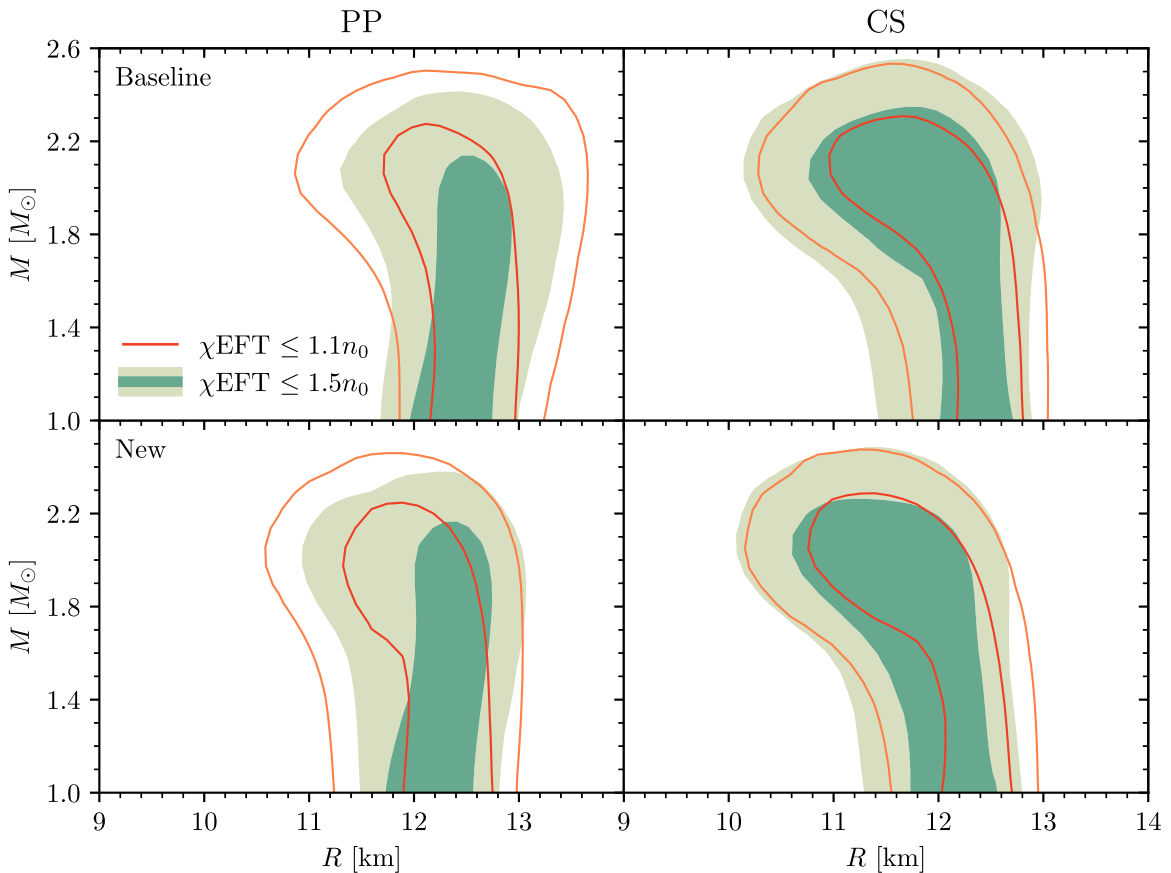


Figure 5. Mass–radius posterior distributions for the “Baseline” (upper panels) and “New” (lower panels) scenarios using the PP (left panels) and the CS model (right panels). The dark (light) green regions and the inner (outer) red curves encompass the 68% (95%) credible regions using the $N^3\text{LO}$ χEFT band up to $1.5n_0$ and $1.1n_0$, respectively.

preferred by the Bayesian evidence, although Vinciguerra et al. (2024) caution that higher-resolution runs are required to check the robustness of the joint NICER-XMM runs. However, the ST+PDT results are more consistent with the magnetic field geometry inferred for the gamma-ray emission for this source (Kalapotharakos et al. 2021, as discussed in Vinciguerra et al. 2024) and the inferred mass and radius for this mode are most consistent with the new results for J0437. For these reasons, we deem this at present—with all reserve and pending further analysis—to be the most likely solution for J0030.

Therefore, the combination of posteriors from ST+PDT for J0030, with Salmi et al. (2024) for J0740 and Choudhury et al. (2024) for J0437, as well as the GW data sets (Abbott et al. 2019, 2020), forms the “New” astrophysical scenario. The impact of the other J0030 solutions is investigated in the Appendix. The GW results are unchanged compared to the “Baseline” scenario, since there are as yet no new mass–tidal deformability results to be included. Figure 4 shows the different mass–radius posteriors used in the “Baseline” and “New” scenarios.

3. Results: Impact of New Prior Distributions and New Astrophysical Constraints

In this section, we investigate the combined impact of the new NICER results and the new $N^3\text{LO}$ χEFT results. We first analyze the posterior inferences on the “Baseline” scenario, to understand how constraining the $N^3\text{LO}$ χEFT calculations are up to a given density. We first analyze the posterior inferences

on the “Baseline” scenario to understand the effects of the different densities up to which the $N^3\text{LO}$ χEFT calculation is trusted. We then compare the inferences on the “New” to the “Baseline” scenario, to study the impact of new astrophysical constraints on the inferred dense matter EOS and neutron star properties. The results for the other χEFT bands and for the sensitivities to the J0030 results are given in the Appendix.

In Figures 5 and 6, we show the mass–radius and pressure–energy density posteriors for the “Baseline” and “New” scenarios, comparing the new χEFT bands at $N^3\text{LO}$ with transition densities $1.1n_0$ and $1.5n_0$. For the CS model, Figure 5 shows that trusting the χEFT results up to $1.1n_0$ and $1.5n_0$ predicts similar mass–radius confidence regions, with the $1.5n_0$ results tending to smaller radii (especially for masses below $1.6M_\odot$) for both the “Baseline” and “New” scenarios. For the PP model, however, trusting the $N^3\text{LO}$ χEFT up to $1.5n_0$ shrinks the radius posteriors compared to $1.1n_0$. Moreover, the mass–radius posteriors predict lower maximum masses when χEFT is trusted up to $1.5n_0$ compared to $1.1n_0$ at the 68% and 95% CIs. Compared to the prior distributions, which include a broad range of softer EOSs with smaller radii, the pressure–energy density posterior distributions in Figure 6 prefer stiffer EOSs to support heavy-mass pulsars and radii around 12.5 km.

We next compare the mass–radius posterior distributions for the “New” scenario to the “Baseline” scenario, leaving the exploration of the effect of the different J0030 results to the Appendix. For the “New” scenario, the mass–radius posterior regions for $1.1n_0$ and $1.5n_0$ in Figure 5 are shifted and/or narrowed to smaller radii

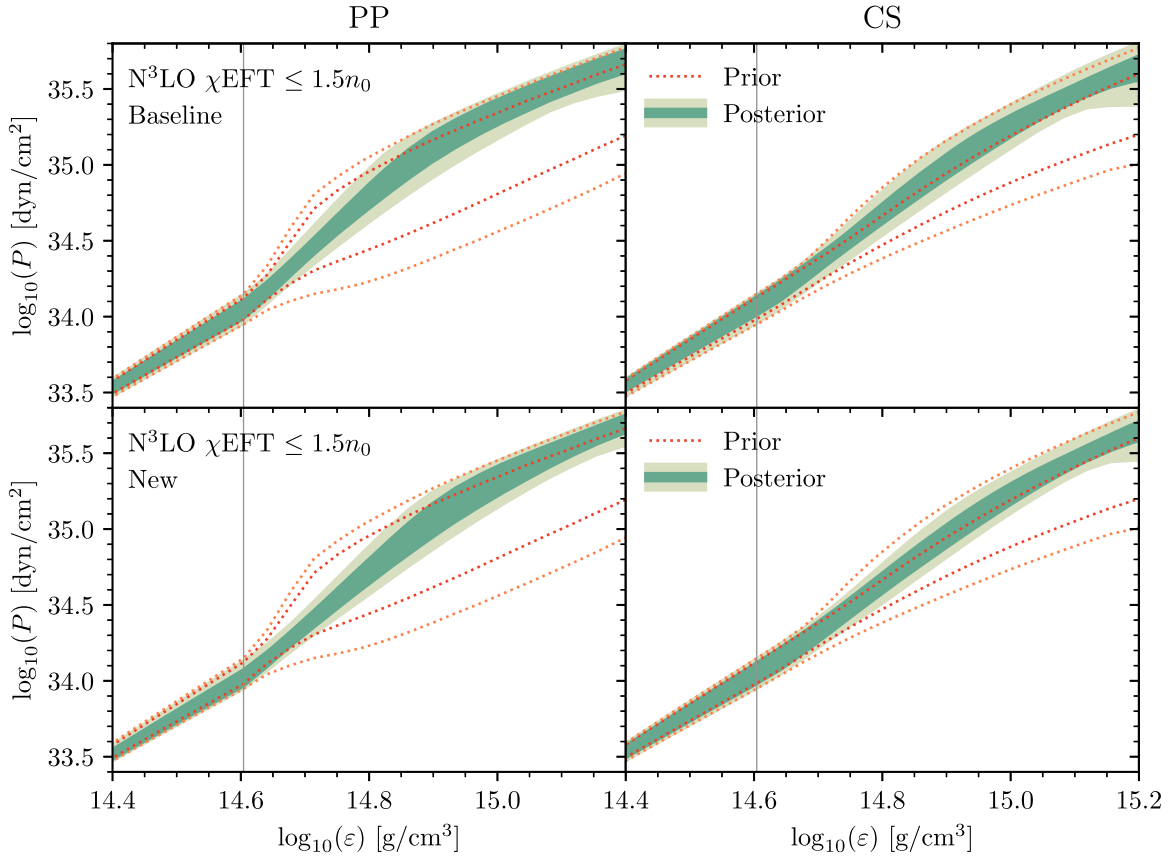


Figure 6. Pressure–energy density posterior distributions for the “Baseline” (upper panels) and “New” (lower panels) scenarios using the PP model (left panels) and the CS model (right panels). The dark (light) green regions encompass the 68% (95%) credible regions, while the dotted red lines represent the corresponding prior distributions using the $N^3\text{LO } \chi\text{EFT}$ band up to $1.5n_0$. The vertical thin lines mark the transition density to the high-density PP and CS extensions.

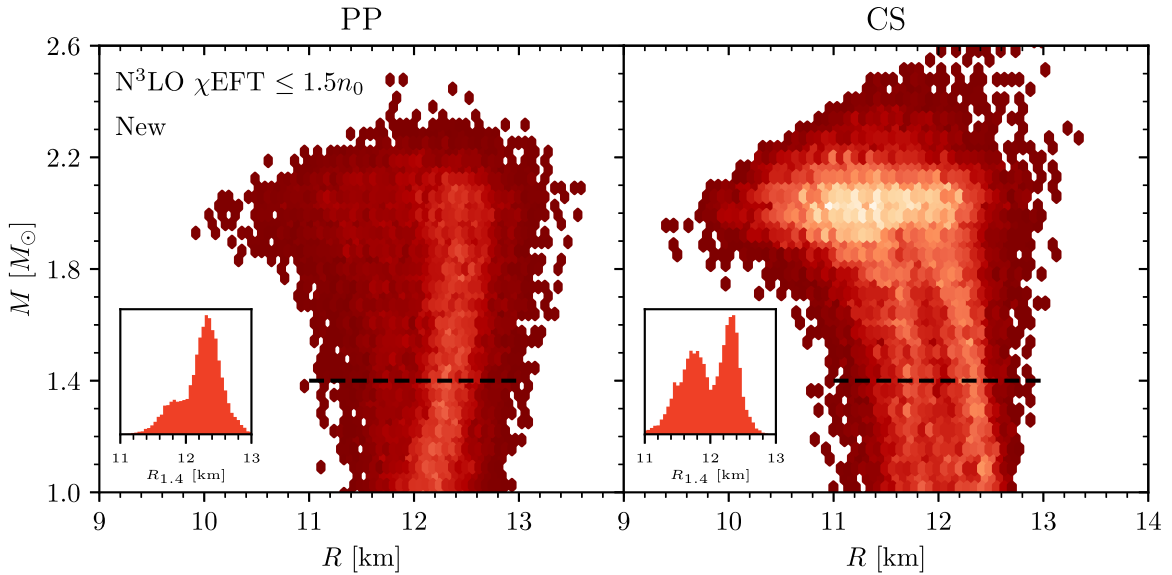


Figure 7. Mass–radius posterior distributions showing the 2D histogram for the “New” scenario using the $N^3\text{LO } \chi\text{EFT}$ band up to $1.5n_0$. The dark shaded hexagons indicate a lower number of mass–radius samples, while the lighter shaded hexagons indicate a higher number of mass–radius samples. The insets show the radius distribution for a $1.4 M_\odot$ star, indicated by the black dashed lines.

compared to the “Baseline” scenario for both the PP and CS models. This shifting/narrowing is due to the addition of the J0437 NICER results as well as to the fact that the J0030 $ST+PDT$ results are consistent with the inferred radius of J0437.

Interestingly, if the $N^3\text{LO } 1.5n_0$ posterior samples of the “New” scenario are cast as a 2D histogram, shown in Figure 7,

the posteriors show hints of a bimodal-like distribution when the new NICER results are folded in. Figure 7 shows a bimodal-like structure centered around 12 km in the CS model. However, for the PP model, the bimodal-like structure is less pronounced.

The bimodal-like distribution also manifests in the posterior distributions of the parameter K , which is the constant that

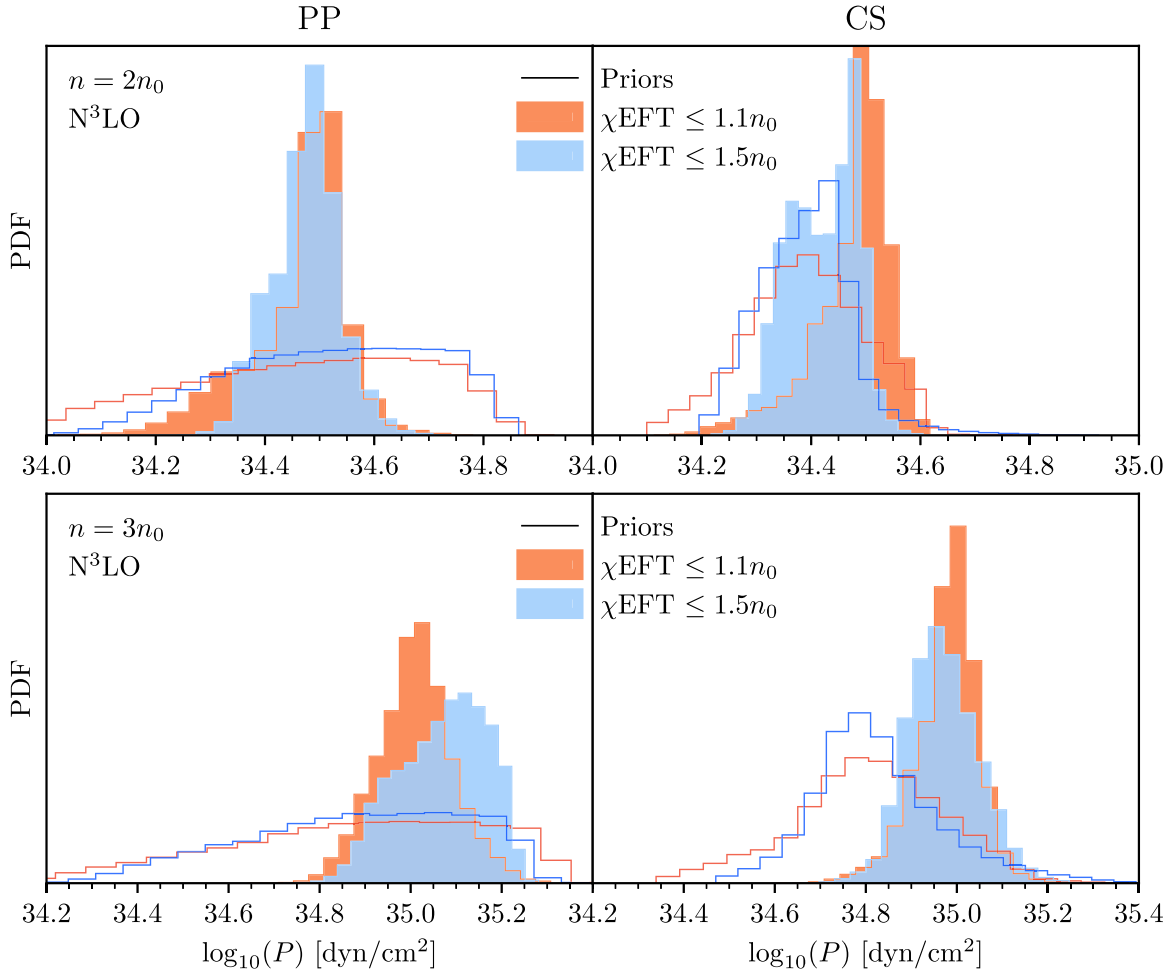


Figure 8. Prior distributions (lines) and posterior distributions (colored regions) for the pressure at $2n_0$ (upper panels) and $3n_0$ (lower panels). Results are shown for the PP model (left panels) and the CS model (right panels) using the χ_{EFT} bands at $N^3\text{LO}$ up to $1.1n_0$ (orange) and $1.5n_0$ (light blue). The posterior distributions are for the “New” scenario.

matches to the χ_{EFT} pressure. Additionally, this structure appears in the pressure posteriors at the intermediate densities $2n_0$ and $3n_0$, plotted in Figure 8. Here, it is clearly present for the $N^3\text{LO}$ $\chi_{\text{EFT}} \leq 1.5n_0$ band for the CS models at $2n_0$, but only hinted at in the PP model at $3n_0$. Despite the bimodal-like structure also being present in the mass–radius posteriors for the $N^3\text{LO}$ $\chi_{\text{EFT}} \leq 1.1n_0$, this effect is not seen in the histogram plots in Figure 8. Additionally, we also find that the bimodal-like distribution is more strongly present with the $N^2\text{LO}$ χ_{EFT} band; see the Appendix for further details. This bimodal-like distribution suggests a tension between the posteriors of J0740, which favor higher radii, and the GW results in combination with J0437, which favor lower-radii posteriors. We also find that this tension is enhanced by the J0030 ST+PDT mass–radius posteriors, due to the strong overlap with J0437.

4. Discussion and Conclusions

In this Letter, we have investigated the constraints on the EOS posed by new joint mass–radius estimates from NICER analysis for J0437 (Choudhury et al. 2024), J0740 (Salmi et al. 2024), and J0030 (Vinciguerra et al. 2024), combined with tidal deformabilities measured during binary neutron star mergers with GWs, and using new χ_{EFT} calculations (Keller et al. 2023) up to $1.5n_0$. In Table 1, we summarize the results, including the constraints on the radius of a 1.4 and $2.0 M_{\odot}$

neutron star, the maximum mass and radius of a nonrotating neutron star M_{TOV} , as well as the central energy density, central density, and pressure for these masses.

4.1. Implications for the Dense Matter EOS

As in Raaijmakers et al. (2021a), we study the changes from the prior to posterior distributions for the pressure at $2n_0$ and $3n_0$ in Figure 8. At densities just above the χ_{EFT} bands, this makes the impact of the astrophysical observations for constraining the dense matter EOS particularly visible. For the PP model at $2n_0$, in Figure 8, the posterior for the pressure is in the central range of the prior, but substantially narrower. In contrast, the CS model prior is already narrower, and the posterior is over a similar range, centered around $10^{34.4}$ dyn cm⁻². This demonstrates the overall consistency among the pressure posteriors for both the PP and CS models. Moreover, as expected, we find a narrower pressure posterior when trusting χ_{EFT} up to $1.5n_0$, especially for the PP model. The pressure posteriors at $3n_0$ are significantly narrowed compared to the broad priors, where the astrophysical results clearly prefer stiffer EOSs at the upper range of the priors in all cases. Additionally, at $3n_0$, the pressures for all χ_{EFT} assumptions consistently predict values centered around 10^{35} dyn cm⁻². Finally, the presence of a bimodal-like structure in some of the pressure posteriors of the $N^3\text{LO}$ χ_{EFT} bands up

Table 1

Key Quantities for the Posterior Distributions for the Different Astrophysical Scenarios

	N ³ LO χ EFT $\leq 1.1n_0$		N ³ LO χ EFT $\leq 1.5n_0$	
	Baseline	New	Baseline	New
PP Model				
$R_{1.4}$	$12.58^{+0.67}_{-0.75}$	$12.30^{+0.55}_{-1.04}$	$12.48^{+0.57}_{-0.67}$	$12.28^{+0.50}_{-0.76}$
$R_{2.0}$	$12.40^{+1.12}_{-1.26}$	$11.99^{+0.93}_{-1.17}$	$12.59^{+0.78}_{-1.24}$	$12.33^{+0.70}_{-1.34}$
ΔR	$-0.16^{+0.48}_{-0.76}$	$-0.28^{+0.47}_{-0.71}$	$0.14^{+0.24}_{-0.77}$	$0.05^{+0.29}_{-0.78}$
M_{TOV}	$2.27^{+0.16}_{-0.26}$	$2.15^{+0.20}_{-0.20}$	$2.17^{+0.15}_{-0.17}$	$2.15^{+0.14}_{-0.16}$
R_{TOV}	$12.03^{+1.51}_{-1.47}$	$11.58^{+1.21}_{-1.21}$	$12.55^{+0.89}_{-1.68}$	$12.22^{+0.83}_{-1.62}$
$\log_{10}(\varepsilon_{c,\text{TOV}})$	$15.13^{+0.26}_{-0.23}$	$15.17^{+0.24}_{-0.20}$	$14.99^{+0.34}_{-0.14}$	$15.04^{+0.31}_{-0.15}$
$n_{c,\text{TOV}}/n_0$	$4.18^{+2.51}_{-1.50}$	$4.52^{+2.40}_{-1.45}$	$3.24^{+2.85}_{-0.79}$	$3.58^{+2.73}_{-0.90}$
$\log_{10}(P_{c,\text{TOV}})$	$35.66^{+0.36}_{-0.35}$	$35.70^{+0.33}_{-0.33}$	$35.44^{+0.48}_{-0.26}$	$35.52^{+0.42}_{-0.26}$
$\log_{10}(\varepsilon_{c,1.4})$	$14.87^{+0.11}_{-0.11}$	$14.91^{+0.11}_{-0.09}$	$14.85^{+0.11}_{-0.08}$	$14.87^{+0.13}_{-0.07}$
$n_{c,1.4}/n_0$	$2.57^{+0.66}_{-0.54}$	$2.80^{+0.78}_{-0.48}$	$2.47^{+0.68}_{-0.38}$	$2.62^{+0.81}_{-0.37}$
$\log_{10}(P_{c,1.4})$	$34.96^{+0.15}_{-0.14}$	$35.02^{+0.18}_{-0.11}$	$34.96^{+0.14}_{-0.10}$	$34.99^{+0.17}_{-0.09}$
$\log_{10}(\varepsilon_{c,2.0})$	$15.02^{+0.21}_{-0.17}$	$15.07^{+0.19}_{-0.15}$	$14.95^{+0.22}_{-0.11}$	$14.99^{+0.23}_{-0.11}$
$n_{c,2.0}/n_0$	$3.43^{+1.75}_{-1.01}$	$3.85^{+1.69}_{-1.0}$	$3.01^{+1.66}_{-0.59}$	$3.27^{+1.86}_{-0.64}$
$\log_{10}(P_{c,2.0})$	$35.39^{+0.32}_{-0.25}$	$35.49^{+0.30}_{-0.22}$	$35.31^{+0.32}_{-0.15}$	$35.37^{+0.35}_{-0.15}$
CS Model				
$R_{1.4}$	$12.44^{+0.41}_{-0.9}$	$12.29^{+0.47}_{-1.03}$	$12.29^{+0.42}_{-0.94}$	$12.01^{+0.56}_{-0.75}$
$R_{2.0}$	$11.91^{+0.8}_{-1.25}$	$11.69^{+0.84}_{-1.12}$	$11.87^{+0.89}_{-1.35}$	$11.55^{+0.94}_{-1.09}$
ΔR	$-0.52^{+0.52}_{-0.76}$	$-0.58^{+0.61}_{-0.73}$	$-0.40^{+0.60}_{-0.82}$	$-0.46^{+0.59}_{-0.76}$
M_{TOV}	$2.11^{+0.28}_{-0.16}$	$2.08^{+0.25}_{-0.17}$	$2.11^{+0.31}_{-0.16}$	$2.08^{+0.28}_{-0.16}$
R_{TOV}	$11.16^{+1.18}_{-1.15}$	$10.97^{+1.17}_{-1.02}$	$11.25^{+1.38}_{-1.32}$	$10.94^{+1.37}_{-1.04}$
$\log_{10}(\varepsilon_{c,\text{TOV}})$	$15.38^{+0.09}_{-0.09}$	$15.38^{+0.09}_{-0.09}$	$15.38^{+0.09}_{-0.14}$	$15.38^{+0.09}_{-0.09}$
$n_{c,\text{TOV}}/n_0$	$6.53^{+1.41}_{-1.11}$	$6.64^{+1.35}_{-1.04}$	$6.65^{+1.51}_{-1.45}$	$6.82^{+1.44}_{-1.30}$
$\log_{10}(P_{c,\text{TOV}})$	$35.89^{+0.24}_{-0.40}$	$35.90^{+0.24}_{-0.37}$	$35.85^{+0.30}_{-0.46}$	$35.88^{+0.27}_{-0.42}$
$\log_{10}(\varepsilon_{c,1.4})$	$14.90^{+0.12}_{-0.07}$	$14.92^{+0.11}_{-0.07}$	$14.91^{+0.12}_{-0.08}$	$14.94^{+0.10}_{-0.09}$
$n_{c,1.4}/n_0$	$2.76^{+0.78}_{-0.38}$	$2.88^{+0.79}_{-0.41}$	$2.83^{+0.83}_{-0.46}$	$3.02^{+0.69}_{-0.51}$
$\log_{10}(P_{c,1.4})$	$35.0^{+0.18}_{-0.09}$	$35.03^{+0.18}_{-0.10}$	$35.02^{+0.18}_{-0.10}$	$35.07^{+0.15}_{-0.11}$
$\log_{10}(\varepsilon_{c,2.0})$	$15.13^{+0.19}_{-0.14}$	$15.16^{+0.18}_{-0.15}$	$15.12^{+0.21}_{-0.17}$	$15.16^{+0.19}_{-0.17}$
$n_{c,2.0}/n_0$	$4.26^{+1.87}_{-1.06}$	$4.49^{+1.79}_{-1.11}$	$4.19^{+2.07}_{-1.18}$	$4.51^{+1.90}_{-1.26}$
$\log_{10}(P_{c,2.0})$	$35.54^{+0.33}_{-0.21}$	$35.58^{+0.30}_{-0.21}$	$35.53^{+0.36}_{-0.24}$	$35.59^{+0.31}_{-0.25}$

Note. Using the N³LO χ EFT bands up to $1.1n_0$ and $1.5n_0$: the radius of a $1.4 M_\odot$ and $2 M_\odot$ neutron star, $\Delta R = R_{2.0} - R_{1.4}$, the maximum mass of a nonrotating neutron star, M_{TOV} , and the corresponding radius to the maximum mass of a nonrotating neutron star, R_{TOV} . We also list the inferred central energy densities ε_c , central densities n_c/n_0 , and corresponding central pressures P_c of M_{TOV} , a $1.4 M_\odot$, and a $2 M_\odot$ neutron star. Radii are given in kilometers, M_{TOV} in M_\odot , and the central energy densities and pressures in grams per cubic centimeter and dyne per square centimeter, respectively. The upper and lower values correspond to the 95% CI.

to $1.5n_0$ (see Section 3) suggests that the inferred neutron star EOS could be described equally well by both a relatively softer or stiffer EOS between $2 - 3n_0$.

An interesting quantity explored in Drischler et al. (2021a) is the difference $\Delta R = R_{2.0} - R_{1.4}$ between the radius $R_{2.0}$ and $R_{1.4}$ of a $2.0 M_\odot$ and $1.4 M_\odot$ neutron star respectively. In particular, Drischler et al. (2021a) pointed out that the sign of ΔR could be an indicator that the underlying EOS softens (if negative) or stiffens (if positive) at high densities. Our results

for ΔR are given in Table 1 and explored with the correlation plot in Figure 9 for the posteriors of our “New” scenario. We find that for the PP model, the preference for ΔR being positive or negative (albeit with large uncertainties) depends on the transition density, but for the CS model, negative ΔR is preferred for all transition densities. Note that Choudhury et al. (2024) reported $\Delta R = 1.13^{+1.59}_{-1.08}$ km (68% CI). At first glance, our inferred ΔR values and the ΔR obtained by Choudhury et al. (2024) appear to be in tension with one another, as our results are centered around $\Delta R = -0.4$ to -0.6 km (CS model) or slightly positive or negative ΔR (PP model). However, the uncertainties are larger and the value quoted in Choudhury et al. (2024) was computed directly from the radius CIs for J0437 and the radius inferred for J0740 by Salmi et al. (2024; subtraction of the median values and simple compounding of the uncertainties), independent of any EOS model. Our results here are derived from the posteriors of the EOS models and their respective priors in addition to the full posteriors for J0030, J0437, J0740, GW170817, and GW190425. These all jointly push the inferred ΔR to smaller central values than the value quoted in Choudhury et al. (2024).

4.2. Implications for Neutron Star Maximum Mass

A key quantity relating to the dense matter EOS is the maximum mass of a nonrotating neutron star, M_{TOV} . This defines the boundary between neutron stars and black holes, and is necessary to our understanding of stellar evolution, supernovae, and compact object mergers.

In Figure 10, we give the joint posterior distribution of M_{TOV} and ΔR for the “New” scenario using the N³LO χ EFT band up to $1.1n_0$ and $1.5n_0$. This shows that the maximum mass is predicted to be below around $2.4 M_\odot$ (95% CI) for all χ EFT assumptions, with slightly larger values for the CS models. Moreover, there is a general trend of increasing M_{TOV} with larger values of ΔR . In addition, in Figure 14 of the Appendix, we observe that the bounds on $M_{\text{TOV}} - \Delta R$ are mostly unaffected when going from N²LO to N³LO and that the bounds on M_{TOV} are very similar for the PP and CS models for both N²LO and N³LO.

In order to assess the impact of the new astrophysical results on M_{TOV} , we show in Table 1 the 95% CIs inferred using the N³LO χ EFT band for both transition densities— $1.1n_0$ and $1.5n_0$ —and both the “Baseline” and “New” astrophysical scenarios. For the PP model, we find that the 95% CI on M_{TOV} is constrained to $2.17^{+0.15}_{-0.17} M_\odot$ and $2.15^{+0.14}_{-0.16} M_\odot$ for the “Baseline” and “New” scenarios, respectively. For the CS model, the “New” M_{TOV} posteriors are again shifted to lower masses when compared to the “Baseline” scenario. In particular, we find that “New” constrains the 95% CI on M_{TOV} to $2.08^{+0.28}_{-0.16} M_\odot$, while the “Baseline” scenario constrains M_{TOV} to $2.11^{+0.31}_{-0.16} M_\odot$. However, despite “New” tending to lower maximum masses, all of the M_{TOV} posteriors strongly overlap, suggesting that the impact of the new astrophysical results on M_{TOV} is small and that it remains strongly dependent on the mass–radius measurements of high-mass pulsars like J0740.

The largest systematic uncertainty in the astrophysical constraints relates to the uncertainty in the inferred mass–radius for J0030, which is now known to have multiple geometric modes with different associated masses and radii. In our analysis, we have considered two different modes identified in Vinciguerra et al. (2024): one for which

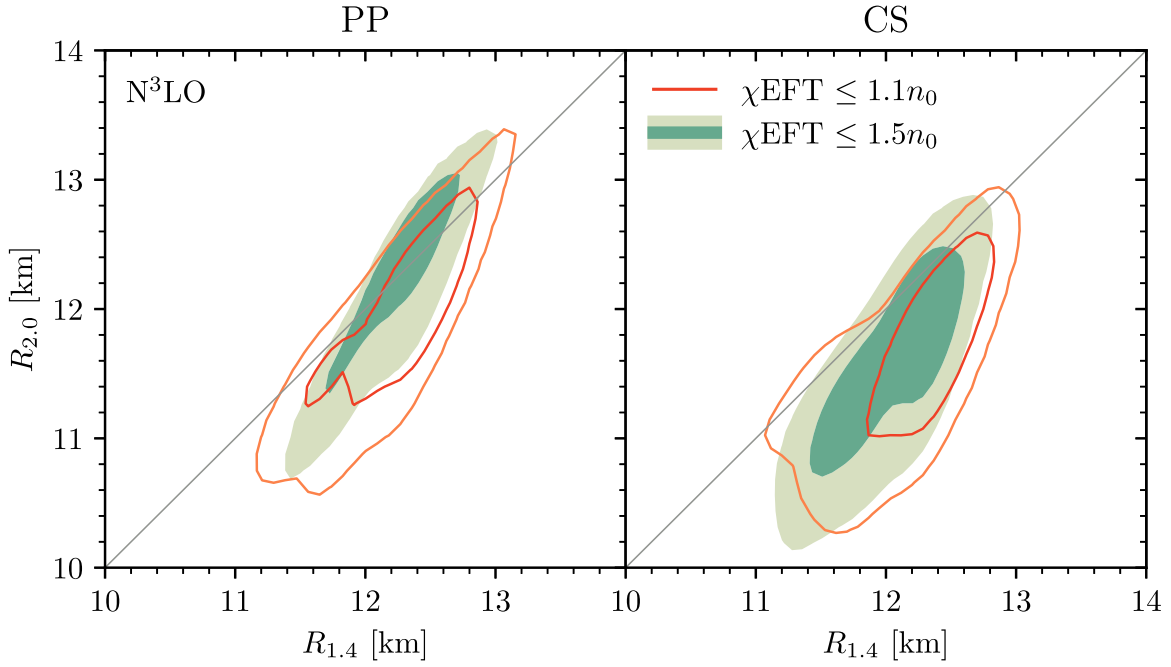


Figure 9. Correlation between the radius $R_{2.0}$ and $R_{1.4}$ of a $2.0 M_\odot$ and $1.4 M_\odot$ neutron star, respectively, for the “New” scenario. Results are shown for the PP model (left panel) and the CS model (right panel) using the χ EFT bands at N³LO up to $1.1n_0$ (red) and $1.5n_0$ (green).

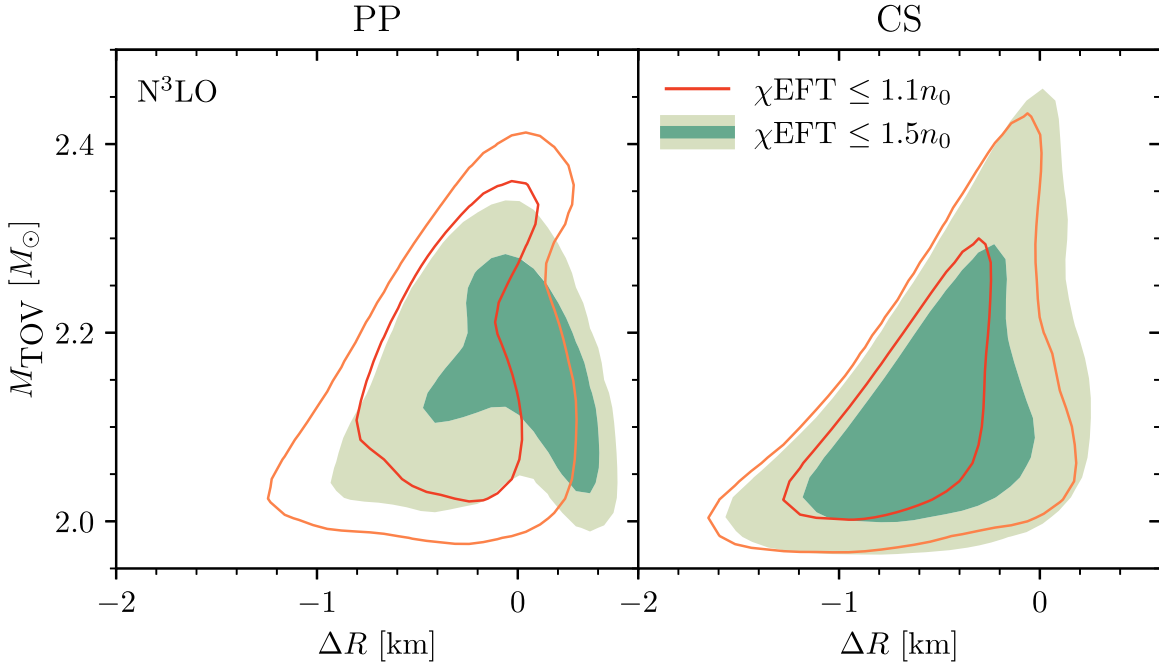


Figure 10. The same as Figure 9, but for the maximum mass M_{TOV} vs. $\Delta R = R_{2.0} - R_{1.4}$.

background constraints are not taken into account (ST+PST) in the “Baseline” scenario, and one mode that emerges when background constraints are applied using joint analysis of NICER and XMM data (ST+PDT) in the “New” scenario. The results in the Appendix, considering other scenarios for J0030, show the sensitivity of the inferred mass–radius to the J0030 results and thus the importance of background constraints. Background constraints are important because by putting bounds on the amount of unpulsed emission coming from other sources, they can rule out certain combinations of hot spot geometry and compactness (see, e.g., Salmi et al. 2022). We cautiously favor the ST+PDT

solution over the PDT–U one, due to its consistency with both the J0437 mass–radius results and multiwavelength pulsar emission models. However, as discussed in Vinciguerra et al. (2024), higher-resolution runs are needed to confirm the robustness of the joint NICER and XMM analysis. Given the anticipated high computational cost, these runs have been deferred, awaiting the preparation of a new larger data set covering all currently available NICER data (Vinciguerra et al. 2024 used a data set consisting of NICER data from 2017 to 2018). Nonetheless, the importance of these posteriors to the dense matter EOS analysis is evident.

4.3. Systematic Uncertainties

Our results are conditional on the choices made for the EOS models and the astrophysical constraints analyzed. The sensitivity of our inferences on the choice of nuclear physics priors is studied by considering the new χ EFT calculations of Keller et al. (2023) at N^3 LO (with N^2 LO studied in the Appendix), trusted up to $1.1n_0$ and $1.5n_0$. As expected, we find that the N^3 LO bands result in tighter posterior constraints when we trust them up to $1.5n_0$. Interestingly, a bimodal-like distribution manifests in the EOS posteriors for both the PP and CS models (see Section 3). Although our inferences suggest that this bimodal-like structure is due to a tension between the posteriors of J0740 and those of J0437 and GW170817, further investigations to better understand its origin are needed, which we leave for future work.

In addition to exploring the sensitivities of the EOS models to the new χ EFT bands, we considered the two different high-density PP and CS extensions. From Table 1, we find that the CS model consistently predicts lower radii for $R_{1.4}$, $R_{2.0}$, and R_{TOV} than the PP model. Therefore, relative to the PP model, the CS model prefers softer neutron star EOSs, in agreement with Raaijmakers et al. (2021a). Table 1 additionally reveals that M_{TOV} , R_{TOV} , and the corresponding central energy densities, central densities, and pressures are noticeably sensitive to increasing χ EFT transition densities in the PP model, but exhibit a much lower sensitivity to the higher transition density in the CS model.

4.4. Summary and Future Prospects

In this Letter, we have studied the impact of the new NICER data and analysis, especially for J0437 and J0740, as well as the choice of J0030 mass–radius posteriors, on the inferred neutron star EOS. Our work shows that the new χ EFT results, especially the extension of the N^3 LO band to $1.5n_0$, tighten the EOS posteriors significantly. In Table 1, we summarize our results of the key quantities for the posterior distributions for the different astrophysical scenarios. In particular, we find the radius of a $1.4 M_\odot$ ($2.0 M_\odot$) neutron star is constrained to the 95% credible ranges $12.28^{+0.50}_{-0.76}$ km ($12.33^{+0.70}_{-1.34}$ km) for the PP model and $12.01^{+0.56}_{-0.75}$ km ($11.55^{+0.94}_{-1.09}$ km) for the CS model, for what we consider our most likely “New” scenario. In this scenario, the maximum mass of neutron stars is predicted to be $2.15^{+0.14}_{-0.16} M_\odot$ and $2.08^{+0.28}_{-0.16} M_\odot$ for the PP and CS models, respectively.

NICER continues to collect more data on all of its targets, including four sources—some of which also have mass priors from radio pulsar timing—for which mass–radius inferences have yet to be published. As we obtain data from more sources and tighter mass–radius inferences, the EOS constraints will continue to improve. New heavy pulsar mass measurements from radio timing and new GW measurements of tidal deformability are also anticipated, with the LIGO–VIRGO–KAGRA collaboration’s next observing run (O4b) starting in 2024 April.

Acknowledgments

This work was supported in part by NASA through the NICER mission and the Astrophysics Explorers Program. The work of C.P.W. and N.R. was supported by NASA grant No. 80NSSC22K0092. The work of K.H., J.K., M.M., A.S., and I.S. was supported by the European Research Council

(ERC) under the European Union’s Horizon 2020 research and innovation program (grant Agreement No. 101020842) and by the Deutsche Forschungsgemeinschaft (DFG, German Research Foundation)—Project-ID 279384907—SFB 1245. A.L.W., D.C., T.S., and S.V. acknowledge support from ERC Consolidator grant No. 865768 AEONS (PI: Watts). Computational work was carried out on the HELIOS cluster, including dedicated nodes funded via this ERC CoG, as well as on the high-performance computing cluster Lichtenberg at the NHR Centers NHR4CES at TU Darmstadt. S.G. acknowledges the support of the CNES. J.M.L. acknowledges support from the US Department of Energy under Grant DE-FG02-87ER40317. We acknowledge extensive use of NASA’s Astrophysics Data System (ADS) Bibliographic Services and the ArXiv.

Appendix

Results for Additional χ EFT Bands and Astrophysical Constraints

In addition to the results for the N^3 LO χ EFT band with the “Baseline” and “New” scenarios discussed in the main text, we provide in the appendix results for the Keller et al. (2023) N^2 LO and the Hebeler et al. (2013) χ EFT band, as well as for two other data scenarios that differ compared to “New” only in the J0030 results from Vinciguerra et al. (2024): “New 2” is based on ST+PST results for NICER data only, while “New 3” is based on PDT+U with a joint analysis of NICER and XMM data. The astrophysical results are summarized in Table 2 and shown as mass–radius regions in Figure 11. All scenarios include the GW results.

A.1. Posterior Results for the “New” Scenario and the Hebeler et al. (2013) and N^2 LO χ EFT Bands

In Figure 12, we show the mass–radius posteriors for the “New” scenario, comparing the previously used Hebeler et al. (2013) band and the Keller et al. (2023) χ EFT bands at N^2 LO and N^3 LO with transition densities of $1.1n_0$ and $1.5n_0$. For the transition density of $1.1n_0$, the top panels of Figure 12 show that the mass–radius posteriors of Hebeler et al. (2013) and N^2 LO predict similar credible regions to the N^3 LO band with only small differences in radii below $1.6 M_\odot$. For the transition density of $1.5n_0$, the N^3 LO χ EFT band is also very consistent with the N^2 LO band, but at N^2 LO we observe a broadening and a hint of a bimodal-like structure more pronounced at N^2 LO than for the N^3 LO band discussed in the main text. Similar to our results for the N^3 LO χ EFT band, the bimodal-like structure also manifests in the posterior distributions of the polytropic fit parameter, K , for the N^2 LO band as well as for the pressure at intermediate densities of $2n_0$ and $3n_0$, as shown in Figure 13.

As discussed in Section 4.2, a key quantity for the dense matter EOS is the maximum mass M_{TOV} . In Figure 14, we give the joint posterior distributions of M_{TOV} and ΔR for the “New” scenario using the N^2 LO χ EFT band up to $1.1n_0$ and $1.5n_0$, which are overlaid with the corresponding N^3 LO posteriors. This shows that the maximum mass is predicted to be below around $2.4 M_\odot$ (95% CI) for all χ EFT assumptions, with slightly larger values for the CS models. Moreover, we observe that the posteriors on $M_{\text{TOV}}-\Delta R$ are largely unaffected when going from N^2 LO to N^3 LO.

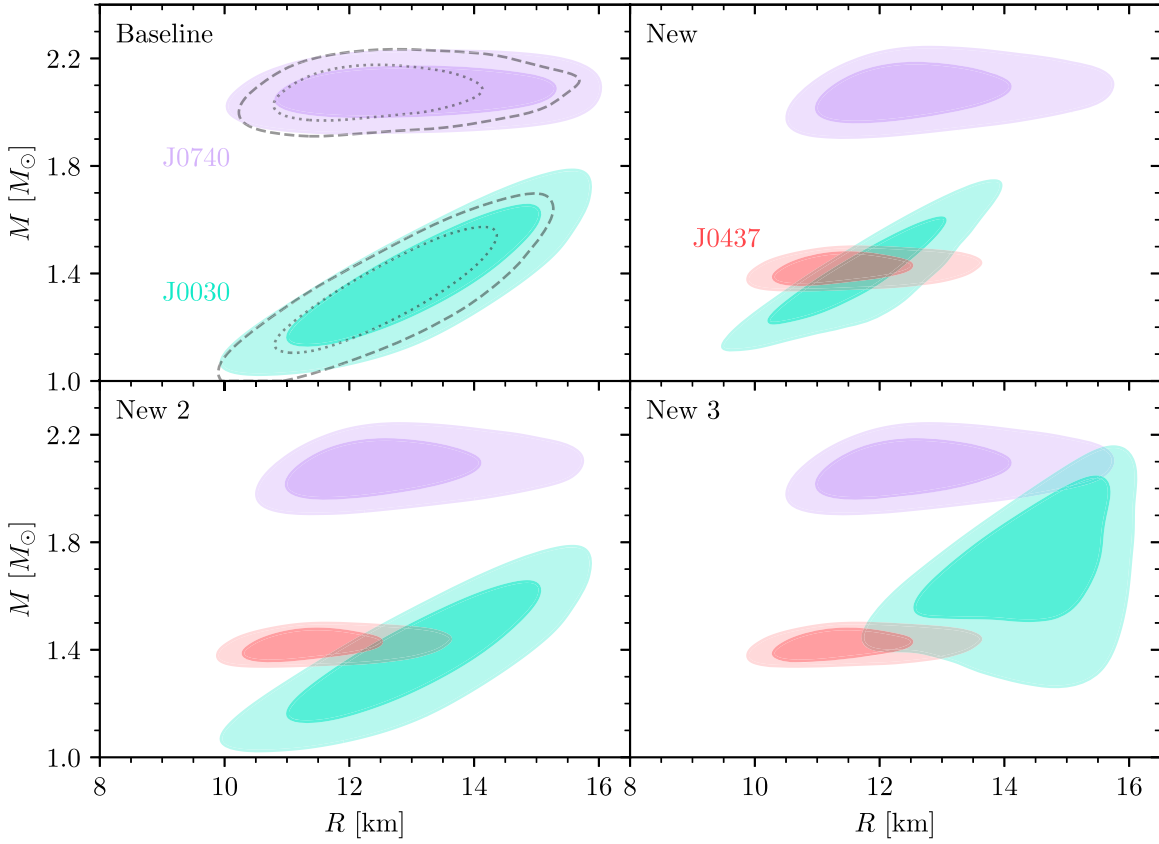


Figure 11. Overview of NICER sources (68% and 95% credible regions for mass–radius), for details see Table 2, with the ‘Baseline’ scenario and the three new scenarios with the new J0437 and J0740 NICER results (Choudhury et al. 2024; Salmi et al. 2024) and exploring the three possible solutions for J0030 from Vinciguerra et al. (2024). For the ‘Baseline’ scenario, we show for comparison the 68% (95%) credible regions from Riley et al. (2019, 2021) as dotted (dashed) lines, which were used in Raaijmakers et al. (2021a).

Table 2
Overview of the Astrophysical Constraints Used in the Baseline and the Three New Scenarios

	GW	J0740		J0030			J0437
	GW170817	ST-U		Vinciguerra et al. (2024)			Choudhury et al. (2024)
	+ GW190425	NICER w bkg Salmi et al. (2022)	NICER \times XMM Salmi et al. (2024)	NICER ST+PST	NICER \times XMM		NICER w bkg CST+PDT
					ST+PDT	PDT-U	
Baseline	×	×	...	×
New	×	...	×	...	×	...	×
New 2	×	...	×	×	×
New 3	×	...	×	×	×

Note. For details, see the text. The abbreviation ‘w bkg’ means ‘with background constraints’. The ‘Baseline’ and ‘New’ scenarios are discussed in the main text. The ‘New 2’ and ‘New 3’ scenarios include different posteriors for J0030 from Vinciguerra et al. (2024).

A.2. Sensitivities to J0030 NICER Mass–Radius Results

We next explore the sensitivities to the J0030 NICER mass–radius results by comparing the ‘New 2’ and ‘New 3’ scenarios to the ‘Baseline’ and ‘New’ scenarios studied in the main text. To this end, we compare in Figure 15 the mass–radius posterior distributions using the N^3 LO χ EFT band up to $1.5n_0$ for the new scenarios to the ‘Baseline.’ Similar to what we found for ‘New,’ the ‘New 2’ mass–radius posteriors shift to somewhat lower radii for the PP model, while for the CS model, the posteriors narrow. This shifting/narrowing of the ‘New 2’ posteriors is due to the combined effect of the J0030 and J0437 NICER results. For the ‘New 3’ scenario, the

posterior distributions narrow slightly compared to the ‘Baseline’ scenario and both the PP and CS models fully remain within the ‘Baseline’ contours. In this case, the J0030 PDT-U results, centered around $R = 14.44$ km, compensate for the J0437 result that pushes the posteriors to lower radii, thus yielding mass–radius posteriors that favor neutron stars closer to 12 km compared to the ‘New’ and ‘New 2’ scenarios. Depending on the choice of whether to include background constraints for J0030 (and the preferred mode once those constraints are included), the mass–radius posteriors (and, by extension, the EOS posteriors) are either—when compared to the ‘Baseline’—marginally unaffected (‘New 2’), pushed

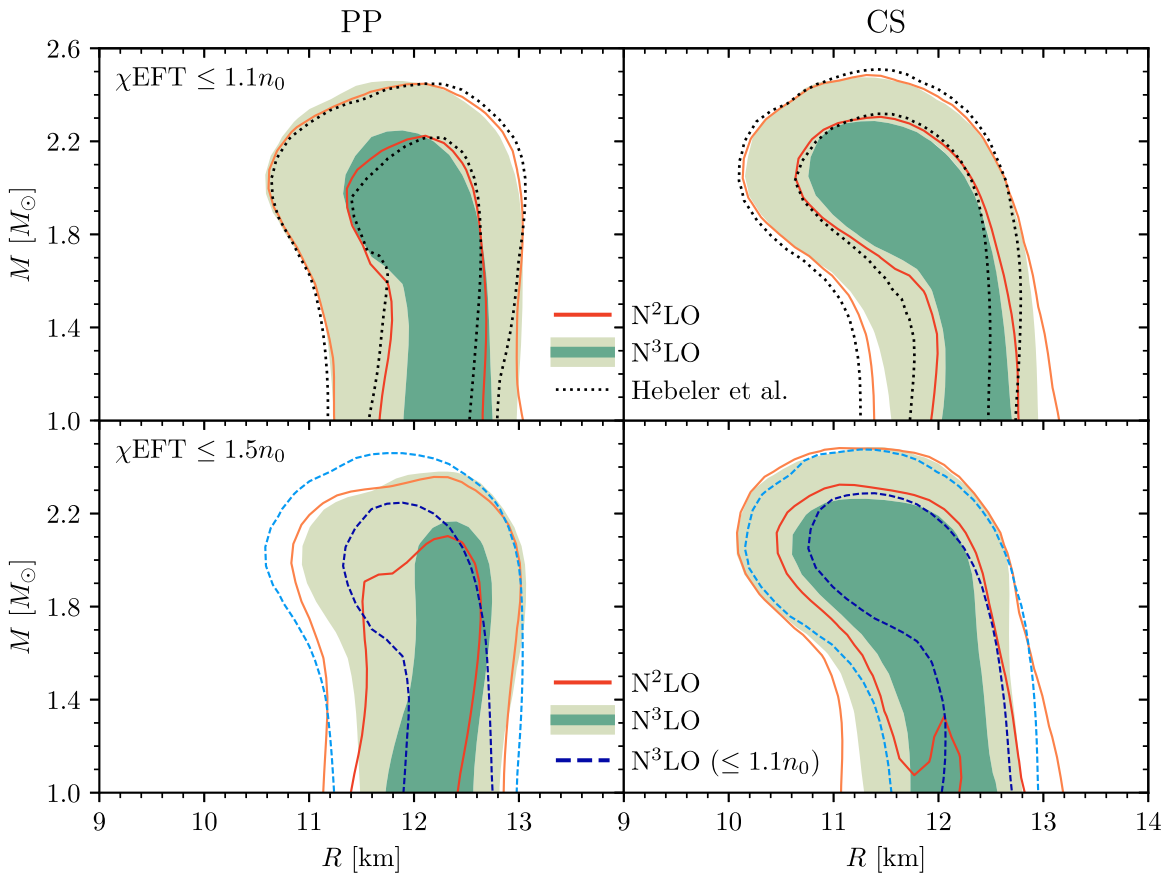


Figure 12. Mass–radius posterior distributions for the PP model (left panels) and CS model (right panels) for the “New” scenario. The dark (light) green region and the inner (outer) curves encompass the 68% (95%) credible regions of the N^3 LO χ EFT band. The top panels compare the posteriors based on the new χ EFT calculations at N^2 LO (red line) and N^3 LO (green bands) from Keller et al. (2023) to those based on the χ EFT calculations from Hebel et al. (2013; dotted black line). For the top panels, the χ EFT bands are used up to $1.1n_0$. In the bottom panels, the posterior distributions are shown when using the new χ EFT calculations up to $1.5n_0$. For comparison, we also show the posterior distribution for N^3 LO used up to $1.1n_0$ (dashed blue lines).

toward lower masses and radii (“New”), or tightened at radii around 12 km (“New 3”). This variation in the inferred neutron star mass–radius relation highlights the dependence of our inferences on the choice of mass–radius posteriors of J0030.

Finally, in Table 3, we list posterior results for the key quantities as in Table 1, but for all four scenarios, using the N^3 LO χ EFT band up to $1.1n_0$ and $1.5n_0$ for both the PP and CS models.

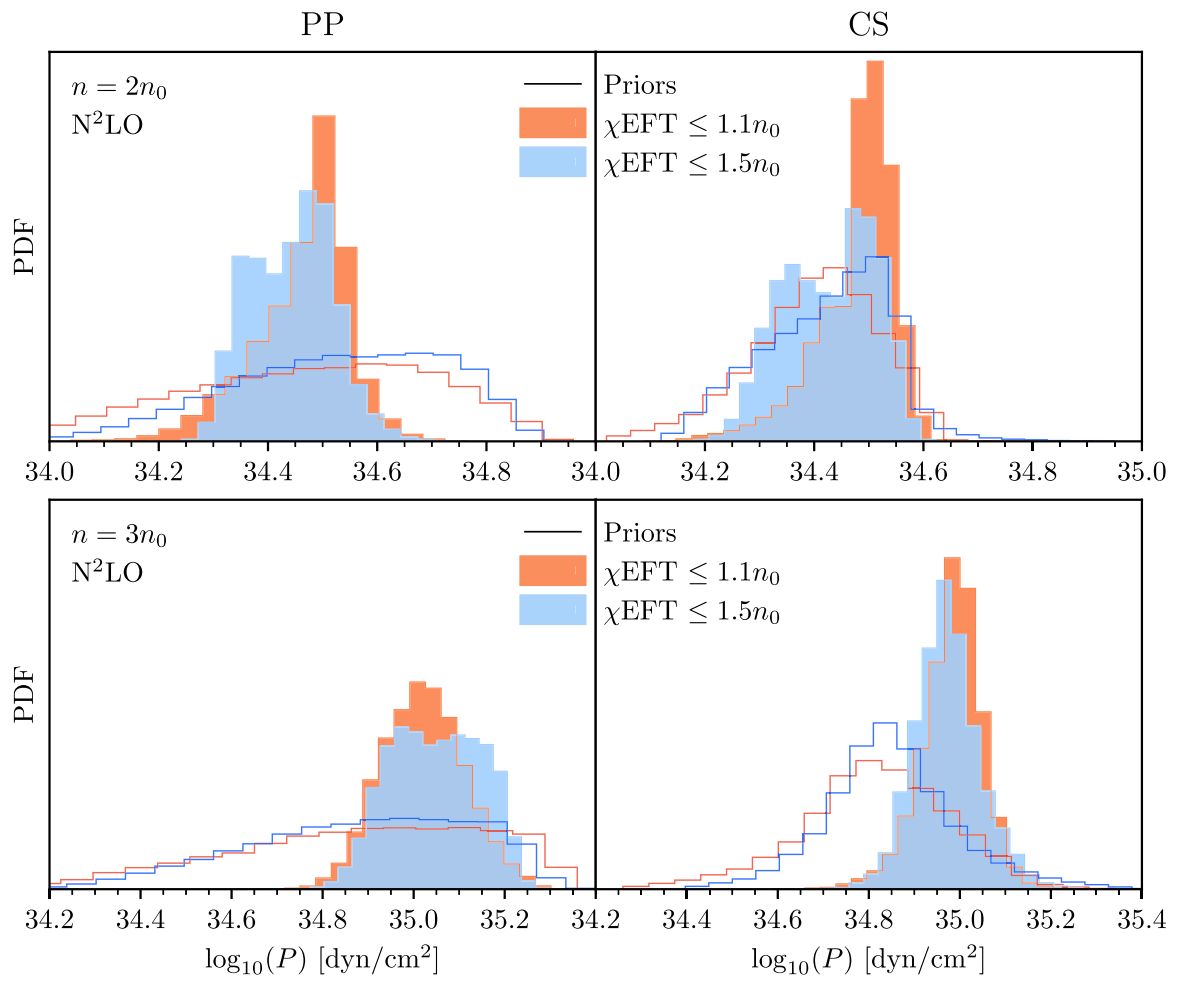


Figure 13. The same as Figure 8, but for N²LO.

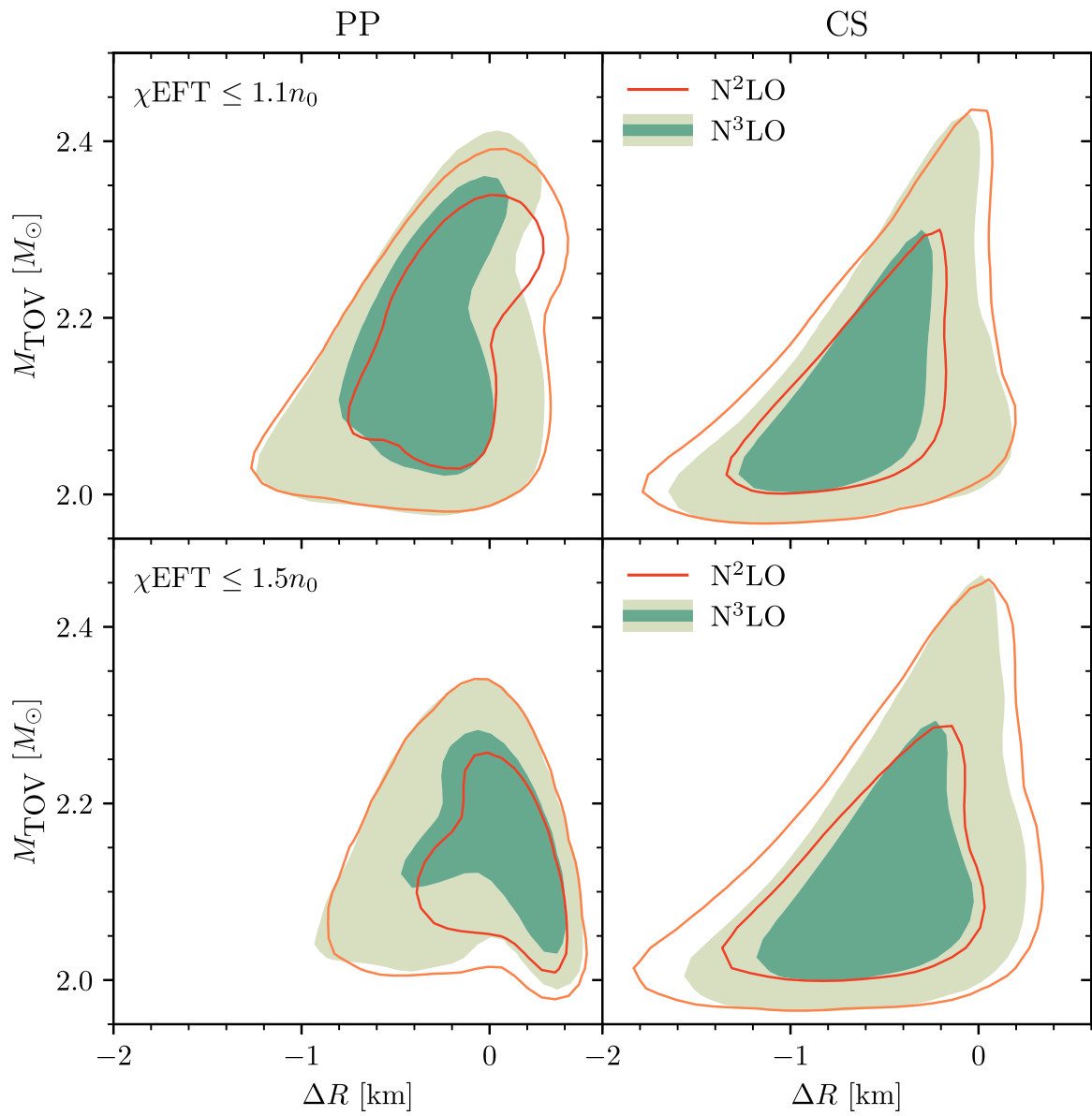


Figure 14. The same as Figure 10, but also including results for the χ^{EFT} bands at $N^2\text{LO}$.

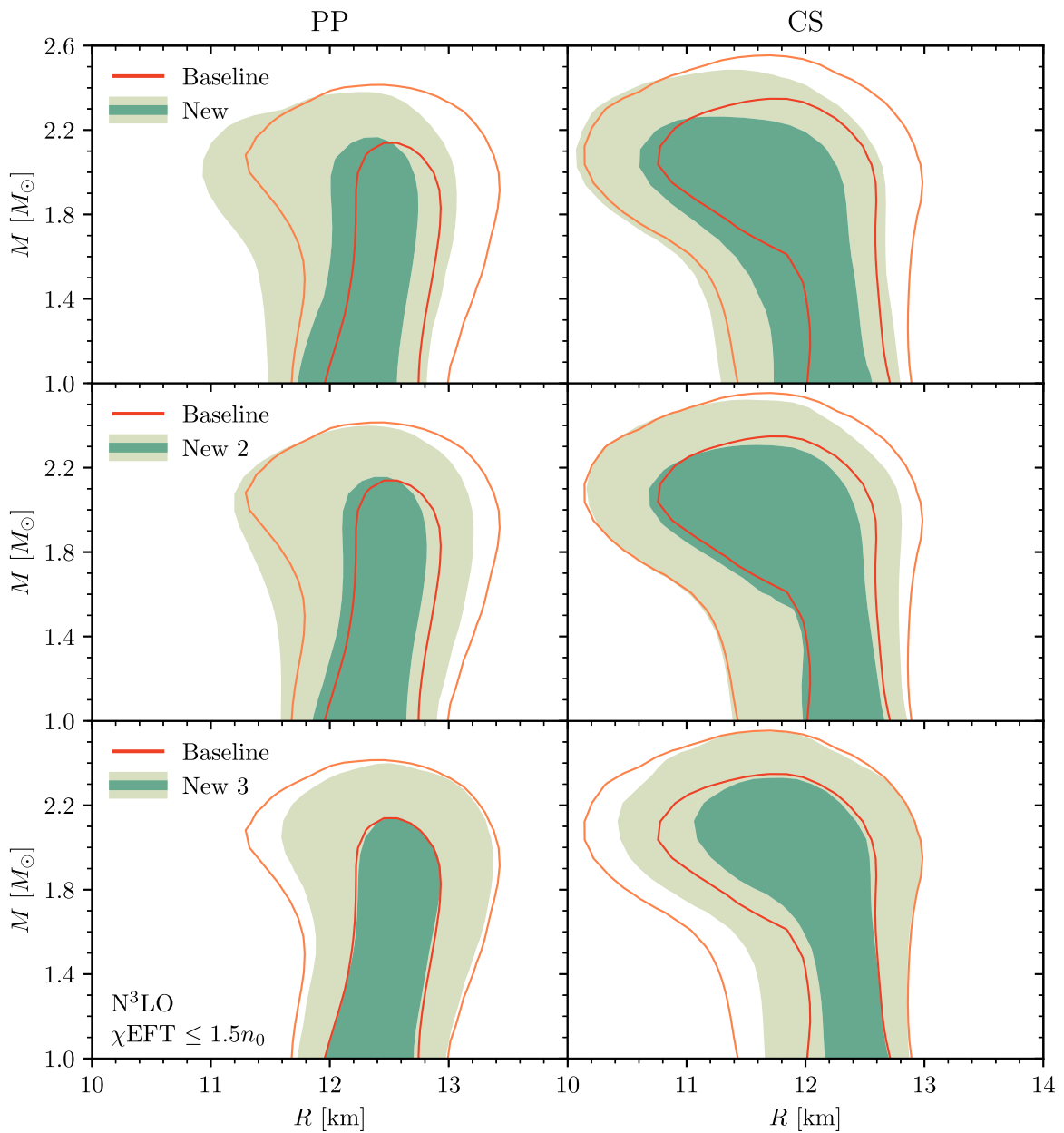

















Figure 15. Mass–radius posterior distributions using the $N^3\text{LO } \chi\text{EFT}$ band up to $1.5n_0$ for the three new NICER scenarios (green shaded regions), in comparison to the “Baseline” scenario (red contours), using the PP model (left panels) and the CS model (right panels). The results using the $N^3\text{LO } \chi\text{EFT}$ band up to $1.1n_0$ are qualitatively very similar.

Table 3
The Same as Table 1, but with Results for the “New 2” and “New 3” Scenarios as Well

	N ³ LO χ EFT $\leq 1.1n_0$				N ³ LO χ EFT $\leq 1.5n_0$			
	Baseline	New	New 2	New 3	Baseline	New	New 2	New 3
PP Model								
$R_{1.4}$	$12.58^{+0.67}_{-0.75}$	$12.30^{+0.55}_{-1.04}$	$12.44^{+0.62}_{-0.95}$	$12.57^{+0.63}_{-0.67}$	$12.48^{+0.57}_{-0.67}$	$12.28^{+0.50}_{-0.76}$	$12.38^{+0.53}_{-0.73}$	$12.47^{+0.56}_{-0.55}$
$R_{2.0}$	$12.40^{+1.12}_{-1.26}$	$11.99^{+0.93}_{-1.17}$	$12.19^{+1.07}_{-1.19}$	$12.41^{+1.05}_{-1.04}$	$12.59^{+0.78}_{-1.24}$	$12.33^{+0.70}_{-1.34}$	$12.46^{+0.73}_{-1.29}$	$12.61^{+0.75}_{-1.02}$
ΔR	$-0.16^{+0.48}_{-0.76}$	$-0.28^{+0.47}_{-0.71}$	$-0.23^{+0.49}_{-0.69}$	$-0.14^{+0.45}_{-0.68}$	$0.14^{+0.24}_{-0.77}$	$0.05^{+0.29}_{-0.78}$	$0.10^{+0.26}_{-0.75}$	$0.16^{+0.22}_{-0.67}$
M_{TOV}	$2.27^{+0.16}_{-0.26}$	$2.15^{+0.20}_{-0.20}$	$2.20^{+0.18}_{-0.23}$	$2.26^{+0.16}_{-0.25}$	$2.17^{+0.15}_{-0.17}$	$2.15^{+0.14}_{-0.16}$	$2.16^{+0.14}_{-0.16}$	$2.16^{+0.15}_{-0.16}$
R_{TOV}	$12.03^{+1.51}_{-1.47}$	$11.58^{+1.21}_{-1.21}$	$11.79^{+1.39}_{-1.28}$	$12.09^{+1.38}_{-1.33}$	$12.55^{+0.89}_{-1.68}$	$12.22^{+0.83}_{-1.62}$	$12.40^{+0.83}_{-1.63}$	$12.58^{+0.84}_{-1.44}$
$\log_{10}(\varepsilon_{c,\text{TOV}})$	$15.13^{+0.26}_{-0.23}$	$15.17^{+0.24}_{-0.20}$	$15.15^{+0.24}_{-0.22}$	$15.11^{+0.26}_{-0.21}$	$14.99^{+0.34}_{-0.14}$	$15.04^{+0.31}_{-0.15}$	$15.01^{+0.31}_{-0.14}$	$14.98^{+0.31}_{-0.13}$
$n_{c,\text{TOV}}/n_0$	$4.18^{+2.51}_{-1.50}$	$4.52^{+2.40}_{-1.45}$	$4.36^{+2.39}_{-1.49}$	$4.06^{+2.41}_{-1.37}$	$3.24^{+2.85}_{-0.95}$	$3.58^{+2.73}_{-0.90}$	$3.38^{+2.66}_{-0.82}$	$3.18^{+2.41}_{-0.73}$
$\log_{10}(P_{c,\text{TOV}})$	$35.66^{+0.36}_{-0.35}$	$35.70^{+0.33}_{-0.33}$	$35.68^{+0.33}_{-0.34}$	$35.64^{+0.35}_{-0.34}$	$35.44^{+0.48}_{-0.26}$	$35.52^{+0.42}_{-0.26}$	$35.47^{+0.43}_{-0.25}$	$35.42^{+0.43}_{-0.23}$
$\log_{10}(\varepsilon_{c,1.4})$	$14.87^{+0.11}_{-0.11}$	$14.91^{+0.11}_{-0.09}$	$14.89^{+0.11}_{-0.10}$	$14.87^{+0.09}_{-0.10}$	$14.85^{+0.11}_{-0.08}$	$14.87^{+0.13}_{-0.07}$	$14.86^{+0.12}_{-0.07}$	$14.85^{+0.10}_{-0.07}$
$n_{c,1.4}/n_0$	$2.57^{+0.66}_{-0.54}$	$2.80^{+0.78}_{-0.48}$	$2.69^{+0.75}_{-0.53}$	$2.57^{+0.55}_{-0.51}$	$2.47^{+0.68}_{-0.38}$	$2.62^{+0.81}_{-0.37}$	$2.54^{+0.76}_{-0.37}$	$2.46^{+0.55}_{-0.36}$
$\log_{10}(P_{c,1.4})$	$34.96^{+0.15}_{-0.14}$	$35.02^{+0.18}_{-0.11}$	$34.99^{+0.17}_{-0.13}$	$34.96^{+0.13}_{-0.13}$	$34.96^{+0.14}_{-0.10}$	$34.99^{+0.17}_{-0.09}$	$34.97^{+0.16}_{-0.09}$	$34.96^{+0.12}_{-0.10}$
$\log_{10}(\varepsilon_{c,2.0})$	$15.02^{+0.21}_{-0.17}$	$15.07^{+0.19}_{-0.15}$	$15.05^{+0.19}_{-0.16}$	$15.01^{+0.19}_{-0.16}$	$14.95^{+0.22}_{-0.11}$	$14.99^{+0.23}_{-0.11}$	$14.97^{+0.22}_{-0.10}$	$14.95^{+0.19}_{-0.10}$
$n_{c,2.0}/n_0$	$3.43^{+1.75}_{-1.01}$	$3.85^{+1.69}_{-1.0}$	$3.65^{+1.62}_{-1.04}$	$3.40^{+1.48}_{-0.94}$	$3.01^{+1.66}_{-0.59}$	$3.27^{+1.86}_{-0.64}$	$3.13^{+1.73}_{-0.60}$	$2.99^{+1.37}_{-0.56}$
$\log_{10}(P_{c,2.0})$	$35.39^{+0.32}_{-0.25}$	$35.49^{+0.30}_{-0.22}$	$35.44^{+0.30}_{-0.24}$	$35.39^{+0.27}_{-0.23}$	$35.31^{+0.32}_{-0.15}$	$35.37^{+0.33}_{-0.15}$	$35.34^{+0.33}_{-0.15}$	$35.31^{+0.27}_{-0.15}$
CS Model								
$R_{1.4}$	$12.44^{+0.41}_{-0.9}$	$12.29^{+0.47}_{-1.03}$	$12.37^{+0.44}_{-0.86}$	$12.48^{+0.37}_{-0.62}$	$12.29^{+0.42}_{-0.94}$	$12.01^{+0.56}_{-0.75}$	$35.34^{+0.33}_{-0.15}$	$12.34^{+0.38}_{-0.73}$
$R_{2.0}$	$11.91^{+0.8}_{-1.25}$	$11.69^{+0.84}_{-1.12}$	$11.81^{+0.81}_{-1.14}$	$11.96^{+0.71}_{-0.97}$	$11.87^{+0.89}_{-1.35}$	$11.55^{+0.94}_{-1.09}$	$11.76^{+0.86}_{-1.18}$	$11.98^{+0.80}_{-1.12}$
ΔR	$-0.52^{+0.52}_{-0.76}$	$-0.58^{+0.61}_{-0.73}$	$-0.56^{+0.53}_{-0.72}$	$-0.51^{+0.47}_{-0.70}$	$-0.40^{+0.60}_{-0.82}$	$-0.46^{+0.59}_{-0.76}$	$-0.43^{+0.58}_{-0.77}$	$-0.36^{+0.55}_{-0.78}$
M_{TOV}	$2.11^{+0.28}_{-0.16}$	$2.08^{+0.25}_{-0.17}$	$2.10^{+0.27}_{-0.16}$	$2.11^{+0.27}_{-0.16}$	$2.11^{+0.31}_{-0.16}$	$2.08^{+0.28}_{-0.16}$	$2.09^{+0.31}_{-0.17}$	$2.11^{+0.31}_{-0.17}$
R_{TOV}	$11.16^{+1.18}_{-1.15}$	$10.97^{+1.17}_{-1.02}$	$11.06^{+1.16}_{-1.01}$	$11.29^{+1.04}_{-0.95}$	$11.25^{+1.38}_{-1.32}$	$10.94^{+1.37}_{-1.04}$	$11.12^{+1.30}_{-1.16}$	$11.40^{+1.28}_{-1.12}$
$\log_{10}(\varepsilon_{c,\text{TOV}})$	$15.38^{+0.09}_{-0.09}$	$15.38^{+0.09}_{-0.09}$	$15.38^{+0.09}_{-0.09}$	$15.38^{+0.05}_{-0.09}$	$15.38^{+0.09}_{-0.14}$	$15.38^{+0.09}_{-0.09}$	$15.38^{+0.09}_{-0.09}$	$15.38^{+0.09}_{-0.14}$
$n_{c,\text{TOV}}/n_0$	$6.53^{+1.41}_{-1.11}$	$6.64^{+1.35}_{-1.04}$	$6.58^{+1.37}_{-1.02}$	$6.49^{+1.16}_{-1.0}$	$6.65^{+1.45}_{-1.51}$	$6.82^{+1.44}_{-1.30}$	$6.70^{+1.51}_{-1.41}$	$6.56^{+1.38}_{-1.35}$
$\log_{10}(P_{c,\text{TOV}})$	$35.89^{+0.24}_{-0.40}$	$35.90^{+0.24}_{-0.37}$	$35.89^{+0.24}_{-0.38}$	$35.85^{+0.26}_{-0.36}$	$35.85^{+0.30}_{-0.46}$	$35.88^{+0.27}_{-0.42}$	$35.85^{+0.29}_{-0.42}$	$35.79^{+0.32}_{-0.42}$
$\log_{10}(\varepsilon_{c,1.4})$	$14.90^{+0.12}_{-0.07}$	$14.92^{+0.11}_{-0.07}$	$14.91^{+0.11}_{-0.07}$	$14.90^{+0.08}_{-0.06}$	$14.91^{+0.12}_{-0.08}$	$14.94^{+0.10}_{-0.09}$	$14.92^{+0.11}_{-0.08}$	$14.90^{+0.10}_{-0.08}$
$n_{c,1.4}/n_0$	$2.76^{+0.78}_{-0.38}$	$2.88^{+0.79}_{-0.41}$	$2.81^{+0.74}_{-0.39}$	$2.72^{+0.53}_{-0.33}$	$2.83^{+0.83}_{-0.43}$	$3.02^{+0.69}_{-0.51}$	$2.90^{+0.76}_{-0.45}$	$2.77^{+0.63}_{-0.41}$
$\log_{10}(P_{c,1.4})$	$35.0^{+0.18}_{-0.09}$	$35.03^{+0.18}_{-0.10}$	$35.01^{+0.17}_{-0.09}$	$34.99^{+0.12}_{-0.08}$	$35.02^{+0.18}_{-0.10}$	$35.07^{+0.15}_{-0.11}$	$35.04^{+0.16}_{-0.09}$	$35.01^{+0.14}_{-0.09}$
$\log_{10}(\varepsilon_{c,2.0})$	$15.13^{+0.19}_{-0.14}$	$15.16^{+0.18}_{-0.15}$	$15.14^{+0.18}_{-0.14}$	$15.13^{+0.17}_{-0.13}$	$15.12^{+0.21}_{-0.17}$	$15.16^{+0.19}_{-0.17}$	$15.13^{+0.20}_{-0.16}$	$15.10^{+0.20}_{-0.15}$
$n_{c,2.0}/n_0$	$4.26^{+1.87}_{-1.06}$	$4.49^{+1.79}_{-1.11}$	$4.39^{+1.78}_{-1.08}$	$4.22^{+1.62}_{-0.97}$	$4.19^{+2.07}_{-1.18}$	$4.51^{+1.90}_{-1.26}$	$4.32^{+1.94}_{-1.18}$	$4.06^{+1.82}_{-1.05}$
$\log_{10}(P_{c,2.0})$	$35.54^{+0.33}_{-0.21}$	$35.58^{+0.30}_{-0.21}$	$35.56^{+0.30}_{-0.21}$	$35.52^{+0.27}_{-0.18}$	$35.53^{+0.36}_{-0.24}$	$35.59^{+0.31}_{-0.25}$	$35.55^{+0.32}_{-0.23}$	$35.50^{+0.31}_{-0.21}$

ORCID iDs

Nathan Rutherford  <https://orcid.org/0000-0002-9626-7257>
 Melissa Mendes  <https://orcid.org/0000-0002-5250-0723>
 Isak Svensson  <https://orcid.org/0000-0002-9211-5555>
 Achim Schwenk  <https://orcid.org/0000-0001-8027-4076>
 Anna L. Watts  <https://orcid.org/0000-0002-1009-2354>
 Kai Hebeler  <https://orcid.org/0000-0003-0640-1801>
 Jonas Keller  <https://orcid.org/0000-0003-2017-4158>
 Chanda Prescod-Weinstein  <https://orcid.org/0000-0002-6742-4532>
 Devarshi Choudhury  <https://orcid.org/0000-0002-2651-5286>
 Geert Raaijmakers  <https://orcid.org/0000-0002-9397-786X>
 Tuomo Salmi  <https://orcid.org/0000-0001-6356-125X>
 Patrick Timmerman  <https://orcid.org/0009-0003-2793-1569>
 Serena Vinciguerra  <https://orcid.org/0000-0003-3068-6974>
 Sebastien Guillot  <https://orcid.org/0000-0002-6449-106X>
 James M. Lattimer  <https://orcid.org/0000-0002-5907-4552>

References

Abbott, B. P., Abbott, R., Abbott, T. D., et al. 2019, *PhRvX*, 9, 011001
 Abbott, B. P., Abbott, R., Abbott, T. D., et al. 2020, *ApJL*, 892, L3
 Alford, J. A. J., & Halpern, J. P. 2023, *ApJ*, 944, 36
 Annala, E., Gorda, T., Hirvonen, J., et al. 2023, *NatCo*, 14, 8451
 Antoniadis, J., Freire, P. C. C., Wex, N., et al. 2013, *Sci*, 340, 448
 Arzoumanian, Z., Brazier, A., Burke-Spolaor, S., et al. 2018, *ApJS*, 235, 37
 Baym, G., Pethick, C., & Sutherland, P. 1971, *ApJ*, 170, 299
 Biswas, B. 2022, *ApJ*, 926, 75
 Bogdanov, S., Dittmann, A. J., Ho, W. C. G., et al. 2021, *ApJL*, 914, L15
 Bogdanov, S., Lamb, F. K., Mahmoodifar, S., et al. 2019, *ApJL*, 887, L26
 Buchner, J., Georgakakis, A., Nandra, K., et al. 2014, *A&A*, 564, A125
 Choudhury, D., Salmi, T., Vinciguerra, S., et al. 2024, *ApJL*, 971, L20
 Cromartie, H. T., Fonseca, E., Ransom, S. M., et al. 2020, *NatAs*, 4, 72
 Dittmann, A. J., Miller, M. C., Lamb, F. K., et al. 2024, *ApJ*, in press, arXiv:2406.14467
 Doroshenko, V., Suleimanov, V., Pühlhofer, G., & Santangelo, A. 2022, *NatAs*, 6, 1444
 Drischler, C., Han, S., Lattimer, J. M., et al. 2021a, *PhRvC*, 103, 045808
 Drischler, C., Hebeler, K., & Schwenk, A. 2019, *PhRvL*, 122, 042501
 Drischler, C., Holt, J. W., & Wellenhofer, C. 2021b, *ARNPS*, 71, 403

- Epelbaum, E., Hammer, H.-W., & Meißner, U.-G. 2009, *RvMP*, **81**, 1773
- Essick, R., Landry, P., Schwenk, A., & Tews, I. 2021, *PhRvC*, **104**, 065804
- Feroz, F., Hobson, M. P., & Bridges, M. 2009, *MNRAS*, **398**, 1601
- Fischer, T., Whitehouse, S. C., Mezzacappa, A., Thielemann, F. K., & Liebendörfer, M. 2010, *A&A*, **517**, A80
- Fonseca, E., Cromartie, H. T., Pennucci, T. T., et al. 2021, *ApJL*, **915**, L12
- Gendreau, K. C., Arzumaniyan, Z., Adkins, P. W., et al. 2016, *Proc. SPIE*, **9905**, 99051H
- Giangrandi, E., Sagun, V., Ivanytskyi, O., Providência, C., & Dietrich, T. 2023, *ApJ*, **953**, 115
- Greif, S. K., Raaijmakers, G., Hebeler, K., Schwenk, A., & Watts, A. L. 2019, *MNRAS*, **485**, 5363
- Hammer, H.-W., Nogga, A., & Schwenk, A. 2013, *RvMP*, **85**, 197
- Harding, A. K., & Muslimov, A. G. 2001, *ApJ*, **556**, 987
- Hebeler, K. 2021, *PhR*, **890**, 1
- Hebeler, K., Lattimer, J. M., Pethick, C. J., & Schwenk, A. 2013, *ApJ*, **773**, 11
- Hebeler, K., & Schwenk, A. 2010, *PhRvC*, **82**, 014314
- Huth, S., Pang, P. T. H., Tews, I., et al. 2022, *Natur*, **606**, 276
- Huth, S., Wellenhofer, C., & Schwenk, A. 2021, *PhRvC*, **103**, 025803
- Janka, H. T., Müller, B., Kitaura, F. S., & Buras, R. 2008, *A&A*, **485**, 199
- Kalapotharakos, C., Wadiasingh, Z., Harding, A. K., & Kazanas, D. 2021, *ApJ*, **907**, 63
- Keller, J. 2023, PhD thesis, Technische Universität Darmstadt
- Keller, J., Hebeler, K., & Schwenk, A. 2023, *PhRvL*, **130**, 072701
- Koehn, H., Rose, H., Pang, P. T. H., et al. 2024, arXiv:2402.04172
- Kurkela, A., Rajagopal, K., & Steinhorst, R. 2024, *PhRvL*, **132**, 262701
- Lattimer, J. M., & Lim, Y. 2013, *ApJ*, **771**, 51
- Lattimer, J. M., & Prakash, M. 2001, *ApJ*, **550**, 426
- Legred, I., Chatziioannou, K., Essick, R., Han, S., & Landry, P. 2021, *PhRvD*, **104**, 063003
- Lim, Y., & Schwenk, A. 2024, *PhRvC*, **109**, 035801
- Lynn, J. E., Tews, I., Carlson, J., et al. 2016, *PhRvL*, **116**, 062501
- Lynn, J. E., Tews, I., Gandolfi, S., & Lovato, A. 2019, *ARNPS*, **69**, 279
- Machleidt, R., & Entem, D. R. 2011, *PhR*, **503**, 1
- Miao, Z., Zhu, Y., Li, A., & Huang, F. 2022, *ApJ*, **936**, 69
- Miller, M. C., Lamb, F. K., Dittmann, A. J., et al. 2019, *ApJL*, **887**, L24
- Miller, M. C., Lamb, F. K., Dittmann, A. J., et al. 2021, *ApJL*, **918**, L28
- O’Boyle, M. F., Markakis, C., Stergioulas, N., & Read, J. S. 2020, *PhRvD*, **102**, 083027
- Pang, P. T. H., Sivertsen, L., Somasundaram, R., et al. 2024, *PhRvC*, **109**, 025807
- Raaijmakers, G., Greif, S. K., Hebeler, K., et al. 2021a, *ApJL*, **918**, L29
- Raaijmakers, G., Greif, S. K., Riley, T. E., et al. 2020, *ApJL*, **893**, L21
- Raaijmakers, G., Nissanke, S., Foucart, F., et al. 2021b, *ApJ*, **922**, 269
- Raaijmakers, G., Riley, T. E., & Watts, A. L. 2018, *MNRAS*, **478**, 2177
- Raaijmakers, G., Riley, T. E., Watts, A. L., et al. 2019, *ApJL*, **887**, L22
- Raaijmakers, G., Timmerman, P., Rutherford, N., et al. 2024, JOSS, submitted
- Radice, D., Burrows, A., Vartanyan, D., Skinner, M. A., & Dolence, J. C. 2017, *ApJ*, **850**, 43
- Read, J. S., Lackey, B. D., Owen, B. J., & Friedman, J. L. 2009, *PhRvD*, **79**, 124032
- Reardon, D. J., Bailes, M., Flynn, C., et al. 2024, *ApJL*, **971**, L18
- Remillard, R. A., Loewenstein, M., Steiner, J. F., et al. 2022, *AJ*, **163**, 130
- Riley, T. E., Choudhury, D., Salmi, T., et al. 2023, *JOSS*, **8**, 4977
- Riley, T. E., Raaijmakers, G., & Watts, A. L. 2018, *MNRAS*, **478**, 1093
- Riley, T. E., Watts, A. L., Bogdanov, S., et al. 2019, *ApJL*, **887**, L21
- Riley, T. E., Watts, A. L., Ray, P. S., et al. 2021, *ApJL*, **918**, L27
- Ruderman, M. A., & Sutherland, P. G. 1975, *ApJ*, **196**, 51
- Rutherford, N., Mendes, M., Svensson, I., et al. 2024, Constraining the Dense Matter Equation of State with New NICER Mass-radius Measurements and New Chiral Effective Field Theory Inputs: Prior and Posterior Samples and Scripts for Generating Plots, v1.1, Zenodo, doi:10.5281/zenodo.10871353
- Rutherford, N., Raaijmakers, G., Prescod-Weinstein, C., & Watts, A. 2023, *PhRvD*, **107**, 103051
- Salmi, T., Choudhury, D., Kini, Y., et al. 2024, *ApJ*, in press, arXiv:2406.14466
- Salmi, T., Suleimanov, V. F., Nättilä, J., & Poutanen, J. 2020, *A&A*, **641**, A15
- Salmi, T., Vinciguerra, S., Choudhury, D., et al. 2022, *ApJ*, **941**, 150
- Salmi, T., Vinciguerra, S., Choudhury, D., et al. 2023, *ApJ*, **956**, 138
- Shakeri, S., & Karkevandi, D. R. 2024, *PhRvD*, **109**, 043029
- Shamohammadi, M., Bailes, M., Freire, P. C. C., et al. 2023, *MNRAS*, **520**, 1789
- Strobel, K., Schaab, C., & Weigel, M. K. 1999, *A&A*, **350**, 497
- Sun, X., Miao, Z., Sun, B., & Li, A. 2023, *ApJ*, **942**, 55
- Suwa, Y., Yoshida, T., Shibata, M., Umeda, H., & Takahashi, K. 2018, *MNRAS*, **481**, 3305
- Takátsy, J., Kovács, P., Wolf, G., & Schaffner-Bielich, J. 2023, *PhRvD*, **108**, 043002
- Tews, I., Krüger, T., Hebeler, K., & Schwenk, A. 2013, *PhRvL*, **110**, 032504
- Vinciguerra, S., Salmi, T., Watts, A. L., et al. 2023, *ApJ*, **959**, 55
- Vinciguerra, S., Salmi, T., Watts, A. L., et al. 2024, *ApJ*, **961**, 62